



**EFFICIENT LAPLACE NMR METHODS FOR
BIOLOGICAL NANOPARTICLES, IONIC LIQUIDS AND
POROUS MATERIALS RESEARCH**

MD SHARIF ULLAH

University of Oulu Graduate school
University of Oulu
Faculty of Science
NMR Research Unit

REPORT SERIES IN PHYSICAL SCIENCES
Report No.149 (2022)

EFFICIENT LAPLACE NMR METHODS FOR BIOLOGICAL NANOPARTICLES, IONIC LIQUIDS AND POROUS MATERIALS RESEARCH

MD SHARIF ULLAH

*University of Oulu Graduate school
University of Oulu
Faculty of Science
NMR Research Unit*

Academic dissertation to be presented with the assent of the Doctoral Training committee of Technology and Natural Sciences of the University of Oulu for public discussion in the auditorium IT116, Linnanmaa, on 01 December 2022, at 12 noon.

REPORT SERIES IN PHYSICAL SCIENCES
OULU 2022 • UNIVERSITY OF OULU

Report No.149

Opponent
Professor Dimitrios Sakellariou

Reviewers
Associate Professor Petrik Galvosas
Dr. Kathryn Anderssen

Custos
Professor Ville-Veikko Telkki

ISBN 978-952-62-3474-8
ISBN 978-952-62-3475-5 (PDF)
ISSN 1239-4327

PUNAMUSTA
VANTAA 2022

Acknowledgments

The research work presented in this thesis was conducted in the NMR Research Unit at the University of Oulu, Finland, starting in 2018 and ending in 2022. I am forever grateful to Professor Ville-Veikko Telkki, the head of the experimental group, for giving me complete access to this perfect NMR facility.

I highly and genuinely appreciate my principal investigator Professor Ville-Veikko Telkki for his role as a mentor throughout my doctoral studies. I am also thankful to him for his help in shaping me as a researcher through his suggestions, innovative approach, and guidance. I could not be more grateful to my co-supervisors, Associate Professor Vladimir Zhivonitko and Dr. Otto Mankinen. Your endless support, extraordinary knowledge, availability, teaching fundamental and advanced NMR, optimism, and ready-to-provide-information attitude helped me complete my thesis. Your encouragement helped me to have a good start and a beautiful end.

I appreciate Dr. Leif Schröder's support and lessons during my research visit to Leibniz Institute for Molecular Pharmacology (FMP) in Berlin, Germany. I am also grateful to Professor Seppo Vainio and Dr. Anatoliy Samoylenko for collaborating on one of my projects and all other co-authors of my articles.

I am deeply grateful to Professor Ville-Veikko Telkki, Dr. Anu Kantola, Associate Professor Vladimir Zhivonitko, Docent Perttu Lantto, and Dr. Sarah Mailhiot for their insightful, exciting, and well-structured NMR lectures in different courses.

I want to express my gratitude to Professor Dimitrios Sakellariou for being my opponent, as well as the pre-reviewers of this thesis, Associate Professor Petrik Galvosas and Dr. Kathryn Anderssen for their insightful remarks. I wish to thank also my follow-up group members, Professor Jürgen Schmidt, Associate Professor Nønne Prisle, and Lecturer Juha Ahola, for their support, cooperation, and efficient participation.

On this journey, I have been accompanied by several individuals. I wish to thank all of them for their role in my journey. Some names are worth mentioning: MSc Yashu Kaharbanda (thanks for being there all the time with me when I needed you and the brotherly relationship we built here), MSc Pau Mayorga Delgado (the talks we had, the NMR studies we did together), Dr. Sarah Mailhiot (for your detailed answers of the things I asked you), Dr. Anne Selent, Docent Perttu Lantto, Dr. Mateusz Urbańczyk, and MSc Perttu Hilla. I wish to extend my gratitude to all the members of the NMR Research Unit. I am also thankful to my doctoral study colleagues: MSc Yashu Kaharbanda, MSc Danila Zakharov, MSc Nazmul Hossain, MSc Anand Chekkottu Parambil, MSc Megha Mohan, MSc Roya Khalili, and Dr. Asadullah Javed.

During my stay, I met some wonderful Bangladeshi people who helped to make my life easier and more comfortable in this harsh-cold-weather and dark nights: Dr. Julius Francis Gomez, Shah Emran, Dr. Md Azmeary Ferdoush, Ehsan Lenin, Joy Bhattacharjee, Gagan Mazed, Dr. Jahangir Alam, Sakhawath Hossain, Tanvir Rahman Lotus, Junayedur Rahman Bhuiyan, Mishad Mohammad, Atiq Mahmud, Mehedi Rabbil, Nipun, Anjan, Asif Iqbal, Z.I. Jony, Rafi Sheikh, Tanzim M Choudhury, Rubel Siddique, Dr. Sanaul Haque, Mohammad Fajus Salehin, Chapal Shaik, Mossabbir Ahmed Himel, and Fahim Tonmoy. They all welcomed me open-heartedly. I wish to thank the Incredible Dr. Julius Francis Gomez for coffee/pulla/leipä and sports discussion time and the knowledge you shared with me at different times. I would like to extend my gratitude to story-teller Dr. Md Azmeary Ferdoush, Fishing-pundit Shah Emran, and Big-brother Ehsan Lenin.

I would like to express my cordial love for some Indian friends: MSc Yashu Kaharbanda, MSc Nazmul Hossain, MSc Anand Chekkottu Parambil, and MSc Sadia Tanweer. I enjoyed our time, the food, and the different occasions together.

No words are enough to express the contribution of my parents and siblings in my life. Their unconditional love and support made it possible to achieve this degree. Maa, your love, inspiration, and dua made this journey smooth for me. Thank you, Baba. You would have been the happiest person among all of us if you were with me today. I miss you, Baba. My deepest gratitude to all my siblings for being there whenever I needed you.

Finally, my loving wife Ayasha Siddka Bristy, your endless support and love helped me to keep everything in line. This achievement is not mine alone. You have as much contribution as I have in this journey. You have tolerated me every single day. You had no complaints even when I was not myself. Your support, love, and care made my journey effortless.

I dedicate my doctoral dissertation to my parents, siblings, and loving wife.

Oulu, Date 24/10/2022

Md Sharif Ullah

Dedicated to my parents, siblings, and loving wife.

Ullah, Md Sharif: EFFICIENT LAPLACE NMR METHODS FOR BIOLOGICAL NANOPARTICLES, IONIC LIQUIDS AND POROUS MATERIALS RESEARCH
NMR Research Unit, University of Oulu, P.O. Box 3000, FI-90014
University of Oulu, Finland
Report Series in Physical Sciences No. 149 (2022)

Abstract

The thesis aims to characterize extracellular vesicles (EVs) utilizing nuclear magnetic resonance (NMR) and develop different ultrafast Laplace NMR (UF LNMR) methods. LNMR consists of diffusion and relaxation NMR experiments and provides detailed information about molecular rotational and translational motion. A multidimensional approach substantially enhances the resolution and information content of LNMR. However, multidimensional LNMR experiments are slow because of the need to repeat the experiment with incremented evolution time. The utilization of an ultrafast approach in multidimensional LNMR experiments significantly reduces the experiment time. In the UF LNMR approach, the evolution times are encoded in different layers of a sample. This way, the data of a multidimensional experiment can be read in a single scan, shortening the experiment time by one to three orders of magnitude. The single scan approach allows hyperpolarization techniques to boost the experimental sensitivity by several orders of magnitude.

In the first part of the thesis, we demonstrate that diffusion-ordered spectroscopy (DOSY) is an NMR tool to characterize various EV samples extracted from milk as well as embryonic kidney and renal carcinoma cells based on their size distributions. The DOSY NMR allows one to determine a broad size distribution ranging from 1 to 500 nm. Transmission electron microscopy (TEM) and nanoparticle tracking analysis (NTA) confirm the DOSY NMR size distribution. However, the NTA analysis cannot detect any particle below 70 nm. A complementary hyperpolarized chemical exchange saturation transfer (hyper-CEST) ^{129}Xe NMR study confirms the presence of small and large nanoparticles in the EV samples.

In the second part of the thesis, we introduced a novel single scan UF LNMR called UF T_2 - T_2 relaxation exchange spectroscopy (REXSY) method to quantify the molecular exchange using T_2 relaxation as a contrast. We studied a halogen-free orthoborate-based ionic liquid (IL) to validate the method. It allowed us to quantify the molecular exchange that occurred between the aggregates and free ions. The results obtained from UF REXSY are in good agreement with conventional reference experiments. The UF REXSY method provides the means of analyzing molecular exchange processes in different fields, such as cellular metabolism and ion transport in electrolytes, with higher sensitivity and efficiency.

In the final part of the thesis, we demonstrated a modified UF T_1 - T_2 correlation experiment suitable for nonlinear sampling of T_1 data. The method leads to the optimal sampling of exponential data. The technique uses frequency-swept pulses whose frequency

increases nonlinearly with time. As proof-of-principle, we exploited the method in analyzing single- and double-tube doped water systems and porous materials. The nonlinear sampling resulted in enhanced resolution. This approach can also be used in other multidimensional UF LNMR experiments, such as diffusion experiments.

Keywords: exosome, extracellular vesicle ionic liquid, silica gel, nuclear magnetic resonance, relaxation, diffusion, DOSY, Laplace NMR, ultrafast LNMR, hyper-CEST.

List of original papers

The present thesis consists of an introductory part and the following papers, which are referred to in the text by their Arabic numerals.

1. M. S. Ullah, V. V. Zhivonitko, A. Samoylenko, A. Zhyvolozhnyi, S. Viitala, S. Kankaanpää, S. Komulainen, L. Schröder, S. J. Vainio, and V.-V. Telkki, 2021. *Identification of extracellular nanoparticle subsets by nuclear magnetic resonance*. *Chemical Science*, 12(24), 8311-8319.
2. M. S. Ullah, O. Mankinen, V. V. Zhivonitko and V.-V. Telkki, 2022. *Ultrafast transverse relaxation exchange NMR spectroscopy*. *Physical Chemistry Chemical Physics*, 24(36), 22109-22114.
3. V. V. Zhivonitko, M. S. Ullah and V.-V. Telkki, 2019. *Nonlinear sampling in ultrafast Laplace NMR*. *Journal of Magnetic Resonance*, 307, 106571.

In Paper 1, the author performed all the NMR experiments and analyses together with V. V. Zhivonitko, S. Komulainen and L. Schröder. In Paper 2, the author carried out all the experiments with O. Mankinen, and analyses were done in cooperation with O. Mankinen and V. V. Zhivonitko. In Paper 3, V. V. Zhivonitko performed all the experiments and analyses together with M. S. Ullah. The author wrote the initial versions of Paper 1 and 2 and contributed to the manuscript of Paper 3. All the authors contributed to the final versions of the manuscripts.

Contents

Acknowledgments	
Abstract	i
List of original papers	iii
Contents	iv
1 Introduction	1
1.1 Background	1
1.2 Outline of the thesis	2
2 Nuclear magnetic resonance	4
2.1 Basics of NMR spectroscopy	4
2.2 Nuclear interactions	6
2.2.1 Chemical shift	6
2.2.3 Other interactions	7
2.3 Relaxation	7
2.3.1 Longitudinal relaxation	7
2.3.2 Transverse relaxation	8
2.4 Diffusion	9
2.5 Multidimensional NMR	10
2.6 Laplace NMR	12
2.7 Ultrafast NMR	14
2.8 Magnetic resonance imaging	16
2.8.1 Frequency encoding	16
2.8.2 Gradient and spin echo imaging	17
2.9 Chemical exchange saturation transfer	18
2.10 Xenon NMR	19
3 NMR analysis of exosomes	22
3.1 Exosomes	22
3.2 Previous NMR studies	23
3.3 DOSY NMR analysis	23
3.3.1 Transmission electron microscopy analysis	25
3.4 ¹²⁹ Xe hyper-CEST NMR analysis	26

4. Ultrafast T_2 - T_2 study of ionic liquids	28
4.1 Ionic liquids	28
4.2 Relaxation and diffusion NMR studies of ionic liquids	29
4.3. Method	29
4.4 Results	30
5. Nonlinear sampling in ultrafast Laplace NMR	34
5.1 Nonlinear sampling	34
5.2 Method	34
5.3 Results	36
6. Summary and conclusions	41
References	43
Original papers	49

1 Introduction

1.1 Background

Nuclear magnetic resonance (NMR) is a powerful analytical tool in science and industry. It provides atomic-level information even if the sample material is opaque. The NMR phenomenon was first reported in the early 1940s by two groups: Purcell, Torrey and Pound (December 1945) [1] and Bloch, Hansen and Packard (January 1946) [2]. These two groups were working independently. Later, both Purcell and Bloch were awarded the Nobel prize for their contribution to Physics in 1952 "for their development of new methods for nuclear magnetic precision measurements and discoveries in connection therewith." Since then, the non-invasive and versatile NMR method has been developed into an essential tool used in materials science, chemistry, biochemistry, medicine, *etc.* Magnetic resonance imaging (MRI), employed by medical practitioners, offers a great deal for diagnostic purposes and is the most well-known application of NMR. In 2003, the contribution of Lauterbur and Mansfield was acknowledged with the Nobel Prize in medicine for their discovery of MRI.

NMR relaxation and diffusion experiments provide detailed information about molecular rotational and translational motion. The experimental data include exponentially decaying components, and the distribution of the relaxation times and diffusion coefficients is solved with the process which is often called the inverse Laplace transformation (a more scientifically precise term could be the inversion of Fredholm's integral of the second kind) [3]. Therefore, the relaxation and diffusion experiments are called Laplace NMR (LNMR). Frydman *et al.* [4–6] introduced spatial encoding, a concept called ultrafast (UF) NMR, for collecting the 2D NMR data in a single shot. The same principles of spatial encoding can also be exploited in multidimensional LNMR [7].

In this thesis, the size distribution of nanosized extracellular vesicles (EVs) secreted from cancer cells and milk were analyzed using diffusion-ordered spectroscopy (DOSY).

Spin-exchange optical pumping (SEOP), an ^{129}Xe hyperpolarization technique combined with chemical exchange saturation transfer (CEST) was used as well to characterize sub populations of extracellular nanoparticles with high specificity and sensitivity. A novel UF relaxation exchange spectroscopy (REXSY) method is introduced. The method facilitates the quantification of molecular exchange between aggregates and free ions of an ionic liquid (IL) sample. In another study, an UF T_1 - T_2 method is modified and tested on water doped with copper chloride in single- and double tubes, and in silica gel. The study gives the opportunity for optimal sampling of T_1 data. The methods introduced offer time-efficient data collection and enhanced resolution. The single scan nature of the experiment makes it easier to boost the sensitivity by exploiting hyperpolarization techniques.

1.2 Outline of the thesis

The thesis consists of two parts. The first part (Chapters 1-2) contains an introduction to NMR and LNMR. The second part (Chapters 3-5) is a summary of the research work, which consists of three peer-reviewed scientific articles at the end.

In Chapter 2, the basics of NMR spectroscopy are introduced. It includes the basics of spectroscopy, relaxation, diffusion, multidimensional and ultrafast NMR as well as 1D MRI.

Chapter 3 focuses on the characterization of EVs of different sources using ^1H DOSY NMR and ^{129}Xe hyper-CEST techniques.

Chapter 4 introduces an ultrafast T_2 - T_2 exchange method.

Chapter 5 describes an approach to UF data collection in a more optimal, nonlinear way, and Chapter 6 summarizes all the published works of the thesis.

2 Nuclear magnetic resonance

Nuclear magnetic resonance (NMR) is a physical phenomenon which occurs when atomic nuclei in a strong, static magnetic field (B_0) are perturbed by a weak, orthogonal oscillating radio frequency (RF) field (B_1). The perturbation causes excitation of nuclear spins only when the oscillating radio frequency matches the resonance frequency of the nuclear spins in the static magnetic field. As a result, an oscillating radio frequency signal, called free induction decay (FID), is observed. The time domain signal is then subjected to a Fourier transform (FT) to obtain frequency domain data, *i.e.*, an NMR spectrum.

NMR techniques do not use ionizing radiation. NMR is a versatile method for studying solid, liquid, and gaseous states of matter. NMR provides detailed structural, spatial, chemical, and dynamic information of a sample. Therefore, NMR is used, for example, in biological and human studies, chemical analysis and industry.

In the following sections, the basic concepts of NMR and a few advanced NMR methods are described. Further details of NMR spectroscopy can be found in the references. [1–4]

2.1 Basics of NMR spectroscopy

Atoms are the basic unit of matter. An atom consists of a positively charged nucleus, which is made up of positively charged protons and neutral neutrons, and a negatively charged electron cloud. Each nucleus has its intrinsic angular momentum vector, \mathbf{J} , also called the spin angular momentum vector. The magnitude of the angular momentum is

$$|\mathbf{J}| = \hbar\sqrt{I(I+1)}, \quad (2.1)$$

where I is the spin quantum number and \hbar is the reduced Planck's constant. I can have values 0, 1/2, 1, 3/2, 2, *etc.* Nuclear spins with a non-zero spin quantum number exhibit magnetic moment

$$\boldsymbol{\mu} = \gamma \mathbf{J}. \quad (2.2)$$

Here, γ is the gyromagnetic ratio of a nucleus. The angular momentum \mathbf{J} and magnetic dipole moment $\boldsymbol{\mu}$ of a nucleus are parallel when the gyromagnetic ratio γ of the nucleus is positive. If the gyromagnetic ratio is negative, then \mathbf{J} and $\boldsymbol{\mu}$ are anti-parallel.

When a nucleus is present in an external magnetic field \mathbf{B}_0 , the interaction between the nuclear magnetic moment $\boldsymbol{\mu}$ and an external magnetic field is called Zeeman interaction, and the interaction energy is

$$E = -\boldsymbol{\mu} \cdot \mathbf{B}_0. \quad (2.3)$$

When \mathbf{B}_0 is parallel to the z-axis of the laboratory frame, the interaction energy becomes

$$E = -\mu_z B_0 = -\gamma \hbar J_z B_0 = -\gamma \hbar m B_0. \quad (2.4)$$

Here, m is the magnetic quantum number, which can have the following values:

$$m = -I, (-I + 1), \dots, (I - 1), +I. \quad (2.5)$$

Therefore, the nucleus has $2I+1$ possible energy levels. The observable transitions have $\Delta m = \pm 1$. Therefore,

$$\Delta E = \gamma \hbar B_0. \quad (2.6)$$

Eq. 2.6 gives the energy required for transition from one energy level to another. The transition can be achieved by electromagnetic radiation with a frequency of

$$\nu = \frac{\Delta E}{h} = \frac{|\gamma|}{2\pi} B_0. \quad (2.7)$$

This is called the resonance frequency or the Larmor frequency.

When a sample including N nuclei is placed in an external magnetic field B_0 , a macroscopic magnetization is formed as the sum of all individual magnetic moments. At thermal equilibrium, the macroscopic magnetization is

$$M_0 = \frac{N\gamma^2 \hbar^2 B_0 I(I+1)}{3kT}, \quad (2.8)$$

where k is the Boltzmann constant, and T is the temperature.

In the beginning of NMR experiments, the macroscopic magnetization is turned away from the z-axis by applying an RF-pulse. The flip angle depends on the duration and strength of the RF pulse. An RF pulse with a 90° flip angle rotates the magnetization into the transverse plane, and an RF-pulse with a 180° flip angle inverts the magnetization in the z-direction. The magnetization vector starts to precess about the direction of the

external magnetic field with the Larmor frequency. The precession of the magnetization vector induces an oscillating current in the detection coil, which is known as the FID signal. A Fourier transform (FT) of the demodulated time domain signal $f(t)$ gives the frequency domain spectrum:

$$F\{f(t)\} = F(\nu) = \int f(t)e^{-i2\pi\nu t} dt. \quad (2.9)$$

2.2 Nuclear interactions

2.2.1 Chemical shift

Electrons around nuclei change the magnetic field. Typically, the magnetic field experienced by nuclei is slightly lower than B_0 . This phenomenon is known as nuclear shielding. The magnetic field at the nuclear site, called the local magnetic field, is

$$B_{\text{loc}} = (1 - \sigma) \cdot B_0, \quad (2.10)$$

where σ is the shielding tensor. Therefore, nuclei in different chemical environments resonate at different resonance frequencies due to the shielding effect. In isotropic liquids, the frequency is

$$\nu = \frac{|\gamma_i|}{2\pi} B_0 (1 - \sigma), \quad (2.11)$$

where σ is the shielding constant. A change in resonance frequency causes a change in the position of the signal, which is called the chemical shift. Consequently, an NMR spectrum reflects molecular structure.

As indicated by Eq 2.11, the resonance frequencies depend on the strength of the external magnetic field. To make spectra measured at different fields easier to compare, a field-independent, dimensionless chemical shift in parts per million (ppm) is introduced:

$$\delta = \frac{\nu - \nu_{\text{ref}}}{\nu_{\text{ref}}} \times 10^6 \approx \frac{\nu - \nu_{\text{ref}}}{\nu_c} \times 10^6. \quad (2.12)$$

Here, ν_{ref} is the frequency of a reference molecule, such as tetramethyl silane, and ν_c is the carrier frequency of a spectrometer.

2.2.3 Other interactions

The interaction between nuclear magnetic moments mediated by bonding electrons is called indirect spin-spin coupling or J-coupling, and it causes the splitting of NMR resonances into multiplets. Dipolar coupling represents the direct interaction between nuclear magnetic moments. Due to isotropic tumbling, the dipolar coupling is not visible in the spectra measured from liquids, but it affects relaxation. Quadrupolar interaction takes place between nuclei with $I > 1/2$ and the electric field gradients (EFG). These interactions are not observable in liquids and gases because of the rapid isotropic tumbling motion of molecules.

2.3 Relaxation

In NMR spectroscopy, relaxation is a fundamental concept which describes the process of returning the magnetization towards the equilibrium state. There are two subcategories of relaxation: spin-lattice relaxation, also known as longitudinal (T_1) relaxation, and spin-spin relaxation, known also as transverse (T_2) relaxation (Figure 2.1). Relaxation is caused by fluctuating magnetic fields that are created by molecular motion. Fluctuating magnetic fields cause both longitudinal and transverse relaxation, but longitudinal relaxation is affected only by transverse fluctuating fields, while transverse relaxation is affected by both longitudinal and transverse fluctuating fields.

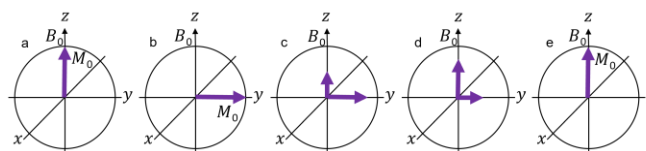


Figure 2.1: Illustration of transverse and longitudinal relaxation in the rotating frame of reference. a) At thermal equilibrium, magnetization is along the external magnetic field direction (the z -direction). b) A 90° pulse rotates the magnetization along the y -axis of the rotating frame of reference. c)-e) Thereafter the transverse magnetization starts to decay and longitudinal magnetization increases due to T_2 and T_1 relaxation, respectively.

2.3.1 Longitudinal relaxation

When a sample is placed in an external magnetic field, magnetic moments tend to align towards the field direction (z -direction), and macroscopic magnetization is built up due to the alignment. The process of approaching the thermal equilibrium magnetization is called spin-lattice relaxation or longitudinal (T_1) relaxation.

When the magnetization is flipped into the transverse plane, the z-component of the magnetization, M_z , which is initially zero, starts to recover back to the equilibrium according to the following equation:

$$M_z(t) = M_0 \left[1 - e^{-\frac{t}{T_1}} \right]. \quad (2.13)$$

Here, T_1 is the longitudinal relaxation time.

T_1 relaxation is usually determined by the inversion-recovery (IR) pulse sequence (Figure 2.2a) [12]. The pulse sequence starts with a 180° rf pulse to invert the thermal equilibrium magnetization. Thereafter, there is a delay τ for the inverted magnetization to recover. After the recovery delay, a 90° read pulse is used to flip the recovered magnetization to the transverse plane for detection. The exponential growth of the M_z magnetization towards its equilibrium state is monitored by repeating the whole process with an incremented τ delay. A short τ delay results in a negative signal and a long τ delay result in a positive signal. In the case of a single relaxation component, the signal observed in the inversion recovery experiment obeys the following equation:

$$M_z(\tau) = M_0 \left[1 - 2e^{-\frac{\tau}{T_1}} \right]. \quad (2.14)$$

Eq. 2.14 is then fitted with the measured signal intensities to the determine T_1 relaxation time. Another way to determine the T_1 relaxation time is to find the time point τ_0 at which the M_z magnetization is zero. According to Eq. 2.14,

$$T_1 = \frac{\tau_0}{\ln 2}. \quad (2.15)$$

2.3.2 Transverse relaxation

In NMR experiments, the magnetization along the external magnetic field is commonly rotated to the transverse plane. Then the magnetization starts to precess with the Larmor frequency around the z-axis. Because of transverse relaxation, the magnetization in the transverse plane starts decaying:

$$M_{xy}(t) = M_0 e^{-\frac{t}{T_2}}. \quad (2.16)$$

In practice, the transverse relaxation decay rate is faster due to magnetic field inhomogeneity [13]. Transverse relaxation time, T_2 , is typically measured using the spin-echo [14] or Carr-Purcell-Meibon-Gill (CPMG) pulse sequence [15]. In the CPMG pulse sequence (Figure 2.2b), the 90_x° excitation pulse rotates the magnetization into the xy-plane (Figure 2.1). Thereafter, the magnetization vectors at different positions start to dephase

due to different local magnetic fields. To overcome this, after the delay τ , a refocusing 180°_y pulse is applied to invert the phases. After another τ delay, the spins are refocused, and an echo is observed. The repetition of 180°_y pulse refocuses the spins again and again, and the echo amplitude decays only due to T_2 . T_2 relaxation time is determined by fitting Eq. 2.16 with experimental data. [2,3]

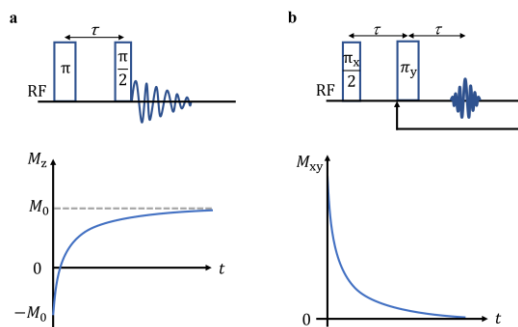


Figure 2.2. a) Inversion recovery and b) CPMG pulse sequences with the corresponding relaxation curves.

2.4 Diffusion

The physical process in which molecules are redistributed in space due to translational Brownian motion, where internal energy acts as the driving force, is called diffusion. Molecular diffusion measurements provide information about physical properties of molecules, such as their sizes and shapes, encapsulation, aggregation, *etc.*

NMR is a standard analytical method for measuring the self-diffusion coefficients of molecules in liquids. It is non-destructive, and molecular self-diffusion coefficients can be measured without tracers. In NMR, diffusion is measured usually by pulsed gradient spin echo (PGSE) [16] (Figure 2.3a) or pulsed gradient stimulated echo (PGSTE) [17] pulse sequences (Figure 2.3b). The PGSE pulse sequence is based on a spin-echo. In the pulse sequence, a short gradient pulse is applied right after a 90° excitation pulse, and it dephases the spins based on their positions. After the gradient pulse, a phase 180° pulse is applied, followed by another identical gradient pulse which rephases the spins. An echo is formed at time 2τ . The time between the two gradient pulses is called diffusion delay (Δ). During the diffusion delay, the spins may change their positions (Figure 2.3c). As a result, the intensity of the signal decreases and the observed signal amplitude is

$$S = S_0 \exp \left[-(\gamma \delta G)^2 D \left(\Delta - \frac{\delta}{3} \right) \right]. \quad (2.17)$$

Here, S_0 is the initial signal intensity at $G=0$, and δ , G and D are the gradient duration, the gradient strength, and the self-diffusion coefficient, respectively. Typically, the pulse sequence is repeated, varying the gradient strength G and keeping the diffusion delay Δ

fixed. The diffusion coefficient is determined by fitting Eq. 2.17 with the experimental data.

The PGSTE pulse sequence (Figure 2.3b) includes three 90° pulses. The first 90° pulse flips the magnetization into the transverse plane and the gradient pulse dephases spins based on their position. The second 90° pulse stores one component of the dephased transverse magnetization along the z-direction. The spoiler gradient between the second and the third 90° pulses removes the residual transverse magnetization. This spoiler gradient dephases the remaining magnetization. The third 90° pulse rotates the stored magnetization back to the xy-plane and it is followed by the second diffusion gradient and reading of the data. If relaxation is not taken into account, the signal intensity in the PGSTE experiment is half of the signal intensity of the PGSE experiment because right after the second 90° pulse, half of the magnetization is dissipated. The relaxation attenuation in the PGSE experiment is dominated by transverse relaxation, whereas in the PGSTE experiment it is dominated by longitudinal relaxation, because the magnetization is stored in the z-direction during Δ delay. Therefore, the PGSTE experiment is more suitable for the samples in which $T_1 \gg T_2$.

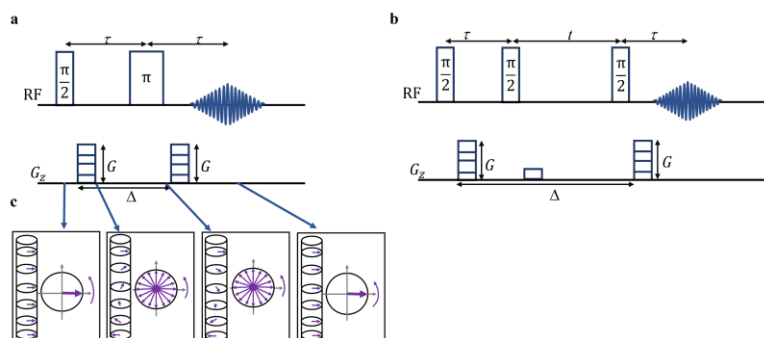


Figure 1.3. a) PSGE, b) PGSTE pulse sequences. c) Behavior of magnetization vectors during the PGSE experiment.

2.5 Multidimensional NMR

In one-dimensional NMR spectroscopy, spectral data are plotted against only one axis. When it comes to multidimensional methods, the intensity of each signal is plotted against two or more axes. Multidimensional NMR experiments are beneficial for achieving more versatile information about the chemical structures and dynamics of molecules. Furthermore, the addition of dimensions in the NMR spectrum improves the resolution.

A basic representation of the two-dimensional NMR experiment (Figure 2.4) has four periods: preparation, evolution, mixing and detection. The preparation period is the beginning of the experiment. This period can have one or more pulses to prepare the magnetization for the next period.

The evolution period starts right after the preparation period ends. In the evolution period, the magnetization evolves with a precession frequency for a time t_1 . The

experiment is repeated many times and t_1 duration is incremented with a fixed value of Δt_1 in each repetition.

Then comes the mixing period, which may include magnetization transfers between spins. At the end of the period, the magnetizations are transferred into an observable signal. Based on the method of choice, many delays, pulses, and gradients may be present during this period.

In the detection period, the signal is recorded for time t_2 .

Overall, the signal in the repeated experiments forms a 2D matrix as a function of time variables t_1 and t_2 . Fourier transformation generates a 2D NMR spectrum, where each row and column separately represent one 1D spectrum in their corresponding frequency axes. Adding more data in the t_2 dimension does not cost a significant amount of experimental time, whereas for one additional data point in the t_1 dimension, an extra repetition is needed. Therefore, multidimensional NMR experiments are more time-consuming when acquired points in the indirect dimension (t_1) are increased.

A broadly used 2D method to study molecular exchange by NMR spectroscopy, known as exchange spectroscopy, (EXSY) [18] was first introduced in 1979. The EXSY method relies on chemical shift contrast. Exchange happens when a molecule moves between different chemical or physical environments. The EXSY method can be used to determine exchange rate. Cross-peaks may appear also due to magnetization transfer caused by the nuclear Overhauser effect (NOE).

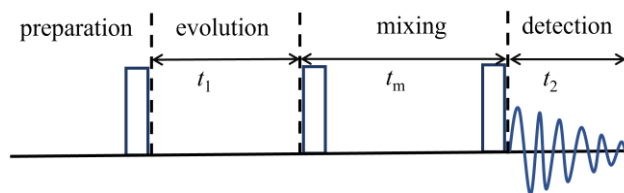


Figure 2.4. 2D EXSY pulse sequence.

The pulse sequence of the EXSY experiments is shown in Figure 2.4. The first 90° pulse flips the magnetization to the transverse plane. Right after the excitation pulse, the evolution period starts. In this period, the spins precess at their precession frequencies and acquire phases. Then the second 90° pulse stores one magnetization component along the z-axis. During the mixing period, the leftover transverse magnetization may be destroyed using a spoiler gradient. Furthermore, the spins may move from one site to another. Then the third 90° pulse flips the magnetization into the transverse plane, and a signal is detected. The experiment is repeated several times with an incremented t_1 value.

Then the collected signal is Fourier transformed to obtain a 2D NMR spectrum. In the spectrum, there can be off-diagonal peaks in addition to diagonal peaks. The off-diagonal peaks arise due to the exchange of spins during the mixing period. The two-dimensional EXSY experiment is an excellent method for studying multisite systems. The sites are resolved in the spectrum when the exchange is slow in the NMR time scale. However, the exchange time should not be longer than longitudinal relaxation T_1 .

2.6 Laplace NMR

Laplace NMR (LNMR) consists of NMR relaxation and diffusion experiments. LNMR can be used to determine the relaxation and diffusion coefficient distributions and unveil information about molecular structures and dynamics. Furthermore, LNMR provides the opportunity to distinguish different components of a system based on their relaxation times and diffusion coefficients. Relaxation and diffusion experiments result in exponentially decaying components; the relaxation time and diffusion coefficient distributions can be extracted from the data by the inverse Laplace transform (ILT) (Figure 2.5) [19]. Relaxation experiments predominantly reflect the random rotational motion of molecules, [20] whereas diffusion measurements uncover information about the translational self-diffusivity of a molecule. The methods are broadly exploited in the study of porous structure of materials. [19,21]

The exponentially decaying signal observed in relaxation and diffusion experiments is presented as

$$S(t) = S(0)e^{-xR}, \quad (2.18)$$

where x represents a variable, and R is the decay rate constant. In relaxation experiments, $x = t$ is time; for instance, in the case of CPMG experiment, $R = 1/T_2$. In the case of the PGSE diffusion experiment, $R = D$ and $x = [(\gamma\delta G)^2(\Delta - \delta^2/3)]$.

The dynamics of a multi-component system may be represented by a relaxation time or diffusion coefficient distribution, $P(R)$. The signal for such a system is

$$S(t) = \int P(R) e^{-xR} dR. \quad (2.19)$$

Eq. 2.19 is similar to the definition of Laplace transform (but $x=t$ is a real number). Therefore, the detected signal $S(t)$ in the relaxation and diffusion experiments is the Laplace transform of $P(R)$. While in the traditional NMR experiment the oscillating FID signal is converted into spectrum by the Fourier transform, in the LNMR experiment the inverse Laplace transform (ILT) is performed to determine relaxation time or diffusion coefficient distribution from exponentially decaying data. [19]

ILT is an ill-posed problem; noisy experimental data can result in an infinite number of distributions of $P(R)$ consistent with the experimental data. For example, two sharp signals with opposite amplitudes next to each other in $P(R)$ produce a negligible contribution to $S(t)$. This problem can be limited using regulators and constraints [22,23]. The most commonly used constraint is the non-negativity constraint, which does not allow negative intensities in relaxation time and diffusion coefficient distributions. Typically, regulators favor smooth and continuous distributions over spiky ones. Depending on the parameter of the regulators, two narrow peaks may turn into one broad peak (oversmoothing), and one broad peak may split into a train of narrower peaks (so-called pearling artefact) [24].

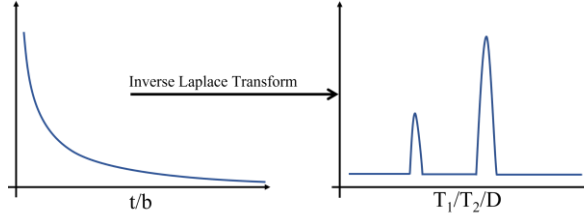


Figure 2.5. Inverse Laplace transform converts an exponentially decaying signal into relaxation time or diffusion coefficient distribution.

Multidimensional LNMR experiments enable the correlation of diffusion coefficients and relaxation times [25,26]. They can also be used in the study of molecular exchange in multisite systems where the sites are not resolved in the spectrum. In order to extract the diffusion coefficient and relaxation time distribution from the experimental data, a robust and reliable multidimensional inverse Laplace transform algorithm is required. [25]

The pulse sequence for a T_2 - T_2 relaxation exchange experiment is shown in Figure 2.6. There are two CPMG loops in the sequence and a mixing time τ_M in between the loops separates them. In the 2D map of T_2 - T_2 exchange experiments, the diagonal peaks appear from the spins having the same T_2 values before and after the mixing period τ_M . Off-diagonal peaks appear in the 2D map if T_2 values change. It happens when the exchange between different sites occurs during the mixing time τ_M . In an experiment, the 2D data set is acquired with an incremented number of CPMG loops in the first part of the sequence. In order to determine the exchange rate, one needs to perform a series of T_2 - T_2 experiments with an incremented mixing time.

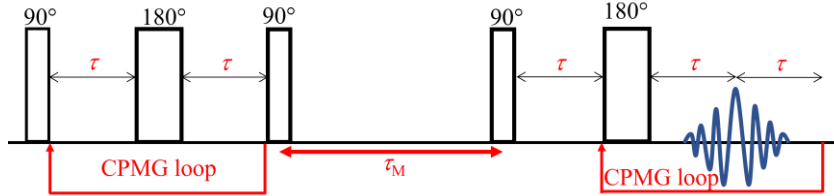


Figure 2.6. Pulse sequence for T_2 - T_2 exchange experiment.

In addition to T_2 - T_2 , there are many other two-dimensional LNMR experiments such as T_1 - T_2 , D - T_2 , T_1 - D and D - D experiments [27,28]. The choice of experiment is based on the system to be investigated and the information to be extracted. The signal observed in a 2D LNMR experiment can be written as

$$S(t_1, t_2) = \iint P(R_1, R_2) e^{-t_1 R_1} e^{-t_2 R_2} dR_1 dR_2. \quad (2.20)$$

Subscripts 1 and 2 refer to the indirect and direct dimensions, respectively. $P(R_1, R_2)$ is the 2D relaxation time or diffusion coefficient distribution and R_1 , R_2 are the decay rate constants.

2.7 Ultrafast NMR

Multidimensional NMR experiments require a long measurement time because the experiment needs to be repeated several times with incremented evolution time or gradient strengths. The concept of UF NMR, based on spatial encoding, was first introduced by Frydman *et al* [4,5,7,29–32]. It enables the collection of 2D data in a single scan. In this approach, the evolution times are encoded into different layers of the sample (Figure 2.7). These experiments shorten the measurement time by one to three orders of magnitude. The spatial encoding can also be exploited to accelerate multidimensional LNMR experiments.

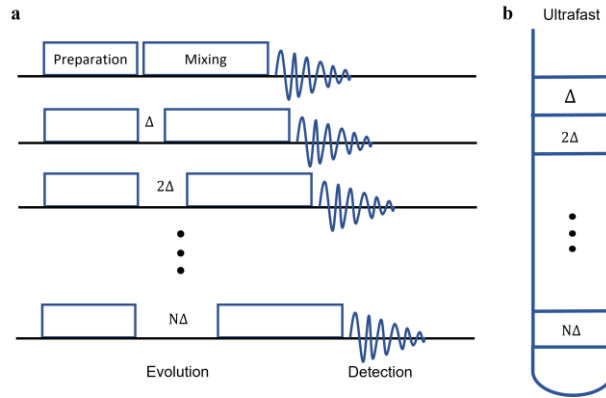


Figure 2.7. a) General scheme for a conventional 2D NMR experiment. The experiment needs to be repeated with incremented evolution delay. b) In an ultrafast experiment, the evolution times are encoded into the discrete layers of the sample, and the data is collected in a single scan.

The evolution times are encoded along the sample layers by applying frequency-swept chirp pulses. The chirp pulse frequency increases/decreases linearly with time:

$$\nu_c = \frac{\Delta\nu}{t_c} t \text{ when } -\frac{t_c}{2} \leq t \leq \frac{t_c}{2}. \quad (2.21)$$

Here, $\Delta\nu$ is the chirp sweep width and t_c is the chirp duration. In the rotating frame of reference, during the sweep, the angle α of the effective magnetic field with respect to the z -axis direction is

$$\alpha(t) = \arctan\left(\frac{\gamma B_1}{2\pi\nu_c}\right), \quad (2.22)$$

where B_1 is the strength of the chirp pulse field. During the chirp pulse, the direction of the effective field changes from the $+z$ -axis to the $-z$ -axis. A strong B_1 field causes the magnetization vector to follow the effective magnetic field adiabatically [8]. The adiabatic condition is fulfilled when

$$|\gamma B_{\text{eff}}(t)| \gg \left| \frac{d\alpha}{dt} \right|. \quad (2.23)$$

Here, B_{eff} is the effective magnetic field. In practice, the adiabatic condition is [4,33]

$$\gamma B_1 \gg \sqrt{\frac{d\nu_c}{dt}} = \sqrt{\frac{\Delta\nu_c}{t_c}}. \quad (2.24)$$

These chirp pulses are used along with the gradient pulses, which make the nuclear Larmor frequency to be linearly dependent on the position:

$$\nu = \frac{\gamma G z}{2\pi}. \quad (2.25)$$

Here, γ is the gyromagnetic ratio, G is the gradient pulse strength, and z is the position along the sample axis. The excitation/inversion time is when the frequency of the chirp pulse and spins match each other and arises from Eqs. 2.21 and 2.25:

$$t(z) = \frac{\gamma G t_c}{2\pi \Delta\nu} z. \quad (2.26)$$

The resonance frequency of the spins depends linearly on the position along the z -axis due to the presence of the gradient. A frequency-swept pulse effects the spins at the bottom first and those at the top last. Therefore, the excitation/inversion time is linearly dependent on the position. The phase of the chirp pulse is

$$\phi_c(t) = \phi_c^0 + 2\pi \int \nu_c dt = \frac{\pi \Delta\nu_c t^2}{t_c}, \quad (2.27)$$

where ϕ_c^0 is the initial phase at time $t = 0$. Eq. 2.27 shows that the phase of the chirp has quadratic time dependency. The x-component of the B_1 field of the chirp is

$$B_{1x} = B_1 \cos(\phi_c). \quad (2.28)$$

As the phase of the chirp pulse varies with time, the spins will experience different phases of the chirp pulse at different times. When a chirp pulse is used to invert the magnetization from $+z$ -axis to $-z$ -axis, the phase does not affect the end result. When a refocusing chirp is used, the result is affected by the phase of the chirp pulse. It needs to be considered when the chirp pulse is designed.

2.8 Magnetic resonance imaging

The clinical imaging method, magnetic resonance imaging (MRI), is the best-known application of NMR. Even though MRI is extensively used for clinical purposes, it is also exploited in many other disciplines, such as chemistry, biochemistry, materials science, *etc.* [34].

2.8.1 Frequency encoding

An MR image is the projection of NMR signals along the spatial axis where a gradient field is applied. The gradient makes a magnetic field vary linearly with position. Therefore, the Larmor frequency of the nuclei depends on the position. The observed signal is processed to obtain an image.

In MRI experiments, when a magnetic field gradient along the x-axis, G_x , is applied, the Larmor frequency ν_0 of the nuclear varies linearly with the x position:

$$\nu = \frac{\gamma(B_0 + xG_x)}{2\pi} = \nu_0 + \frac{\gamma x G_x}{2\pi}. \quad (2.29)$$

When a gradient is applied and an FID is observed, the FID contains information on the position of spins along the applied gradient field direction. The Fourier transformation of the FID is now the frequency distribution of a signal and is the 1D image of the sample.

The frequency axis can be converted into the spatial locations by using the following equation:

$$x = \frac{2\pi(\nu - \nu_0)}{\gamma G_x}. \quad (2.30)$$

The observed 1D MRI signal is

$$S(k) = \int \rho(r) e^{-i2\pi kr} dr. \quad (2.31)$$

Here, $\rho(r)$ is the effective spin density, and k is the spatial frequency

$$k(t) = \frac{\gamma}{2\pi} \int G(t) dt, \quad (2.32)$$

where $G(t)$ is the gradient as a function of time. The Fourier transform of the 1D MRI signal (Eq. 2.31) provides the 1D image (the spin density distribution, Figure 2.8):

$$\rho(r) = \int S(k) e^{i2\pi kr} dk. \quad (2.33)$$

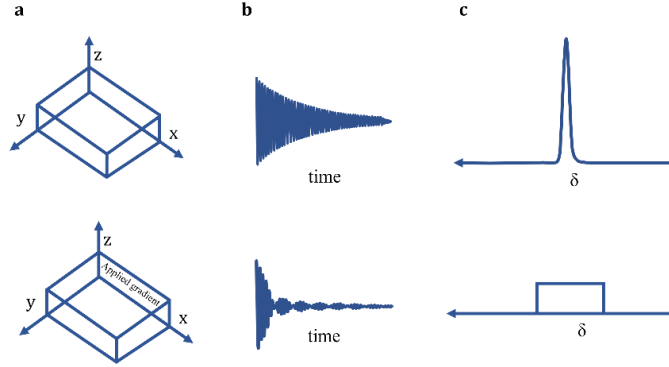


Figure 2.8. The spectra of a water-filled square box with and without gradient. a) The water-filled box without and with the gradient along the x-axis. b) Resulting FIDs of the experiments. c) Corresponding Fourier transformed spectra. In the absence of a gradient, a sharp peak is observed. With the applied gradient, the spectrum looks like a flat rectangle, a 1D image.

2.8.2 Gradient and spin echo imaging

Gradient echo and spin echo are the most commonly used methods in MRI. In gradient echo imaging (Figure 2.9a), an excitation pulse with a small flip angle α is typically used. According to the Ernst rule [35], the maximum signal is obtained in a fixed time when the flip angle is

$$\cos \alpha = e^{-\frac{t_0}{T_1}}, \quad (2.34)$$

where t_0 is the repetition time to accumulate more signals in a multi scan experiment.

The first gradient with a negative amplitude causes a shift from the center of k -space to a negative maximum, $-k_{\max}$ (from position 1 to 2) and dephasing of the spins. Thereafter, a positive read gradient with a double area is applied and the signal is read. The read gradient rephases spins and gradient echo is formed at the center of the gradient.

Two RF pulses are used in the case of 1D spin echo imaging (Figure 2.9b). The first gradient after the initial 90° excitation pulse causes a shift from the center of k -space (1) to a positive maximum (2), k_{\max} . After the τ delay, the 180° pulse inverts the phases of the spins and the k -value from k_{\max} (2) to $-k_{\max}$ (3). Then the signal is acquired in the presence of a read gradient and an echo is observed after another τ delay. During the acquisition time, k -values change from position 3 to position 4. In this method, both the spin echo and the gradient echo are formed simultaneously at the center of the read gradient and the magnetic field inhomogeneity is refocused.

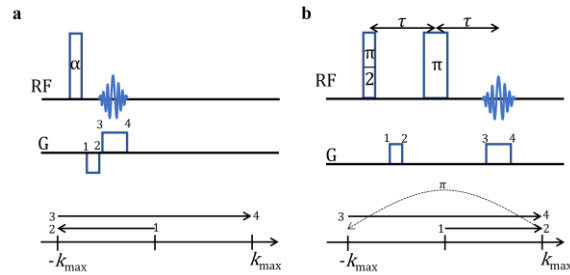


Figure 2.9. a) Gradient echo b) spin echo 1D imaging pulse sequences and their k -space trajectories.

2.9 Chemical exchange saturation transfer

NMR spectroscopy is a rather insensitive method. Chemical exchange saturation transfer (CEST) offers the means to investigate the exchange processes. Furthermore, the method may enhance the sensitivity by orders of magnitude via chemical exchange saturation transfer, making low spin population pools observable. In CEST experiments, the requirement is the existence of exchangeable pools, where the exchange is slow in the same NMR time scale.

The CEST experiment begins with a continuous wave (CW) saturation pulse (Figure 2.10a). After saturation, the spectrum is measured by using a hard pulse (90°). Let's assume that the spectrum includes two signals (Figure 2.10b): a minor signal arising from encapsulated Xe (circle in a triangle), and a major signal arising from the unbound Xe (circle). If the CW frequency matches with the frequency of encapsulated Xe, the signal from encapsulated Xe becomes saturated (Figure 10c). If exchange occurs, the saturated encapsulated Xe atoms are then transferred to the unbound Xe pool, leading to an attenuation in the free Xe signal (Figure 2.10d). There is a continuous replacement of saturated Xe atoms by non-saturated Xe atoms in the encapsulated pool, and the non-saturated Xe atoms are always saturated due to the continuous saturation. This leads to an accumulation of saturated Xe atoms in the free Xe pool, causing a significant reduction of the signal intensity (Figure 2.10d). This allows significantly enhanced indirect measurement of a free Xe pool. The decrease of the signal intensity of the major Xe signal as a function of CW saturation frequency is represented as the CEST (or Z-) spectrum (Figure 2.10e) [36].

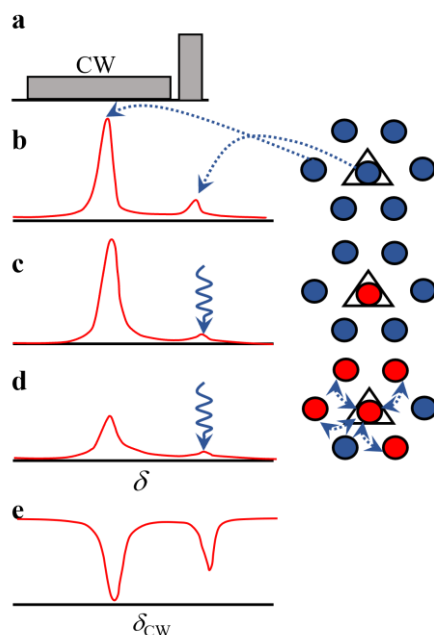


Figure 2.10. An illustration of the chemical exchange saturation transfer experiment. a) CEST pulse sequence. The effect of a continuous wave (CW) saturation pulse on observed spectrum b) before, c) in the beginning and d) at the end of the CW pulse. e) CEST spectrum, *i.e.*, the amplitude of the unbound Xe signals as a function of saturation frequency offset. Blue and red circles represent polarized and saturated Xe atoms, respectively. Triangles represent encapsulated sites. The saturation frequency is indicated with the wavy blue arrow. The double-headed blue arrows show the exchange between the sites.

2.10 Xenon NMR

The NMR active xenon (Xe) nuclei are ^{129}Xe and ^{131}Xe . The spins of ^{129}Xe and ^{131}Xe are $1/2$ and $3/2$, and the natural abundances of these isotopes are 26% and 21%, respectively. ^{129}Xe is the Xe isotope that is primarily used in NMR because it is a spin- $1/2$ nucleus and has higher sensitivity compared to ^{131}Xe [36]. Xenon is an inert and monoatomic gas. It has a relatively large spherical electron cloud, which makes the ^{129}Xe chemical shift very sensitive to its local environment. Xe has been used to investigate extracellular vesicles, membranes, porous media, cages in zeolites, clathrates, polymers, *etc.* [36–42]

NMR sensitivity can be enhanced by utilizing the spin-exchange optical pumping (SEOP) [43] technique by several orders of magnitude. In SEOP, a mixture of alkali-metal vapor, most often rubidium, and noble gas (Xe) is used. In the first step, a circularly polarized light with an appropriate wavelength is used in the presence of an external magnetic field to polarize rubidium. Thereafter, during binary collision, the hyperfine

interaction between the rubidium electron and Xe nucleus occurs and transfers the spin-polarization from rubidium to Xe. [43]

In ^{129}Xe hyper-CEST experiments, a selective-saturation pulse is applied to the low Xe-populated pool. The saturated xenon atoms are transferred to the bulk Xe pool, and an exchange between the saturated and non-saturated Xe occurs. Due to this, there is a slight signal attenuation of the bulk Xe pool. The continuation of Xe saturation and exchange results in a substantial bulk signal attenuation and leads to indirect detection of low population Xe pool.

3 NMR analysis of exosomes

3.1 Exosomes

Exosomes, which are a subclass of extracellular vesicles (EVs), are nanosized biological particles that are 30-150 nm in diameter [44,45]; they are released from multicellular organisms into the extracellular environment. Over the last few years, exosomes have received attention for their abundance and role in the physiological processes of multiple multicellular organs. The important feature of these vesicles is that they transfer compounds such as lipids, proteins, DNA, mRNA, and miRNAs to target cells; that is why they are also called signalosomes [46,47]. Some known functions of exosomes are immune response [48], mediating cell-to-cell signaling, and acting as a bioactive molecules transporter [49]. In addition to that, they have some properties such as low toxicity, biological membrane permeability, inherent stability, biocompatibility, and low immunogenicity, which are the most critical factors for choosing any biosystem for a drug delivery cargo [49]. Lipids and proteins available at the surface of exosomes act as a biomarker and specify their target and origin of secreting cells. This feature also helps to differentiate different proteins present in exosomes and use them as a potential tool for diagnosing diseases like cancers [50]. Therefore, the characterization of exosomes is necessary for the treatment of such conditions.

The biogenesis of exosomes involves the following: formation of endocytic vesicles, multivesicular bodies (MVBs) formation, and the fusion of the MVBs [51]. In the beginning, a cup-shaped structure is formed by the invagination of the endosomal membrane. This contains extracellular surface protein, a membrane-bound signalling protein, soluble protein, lipid rafts, *etc.*, which paves the way for the formation of early-sorting endosomes (ESE). Contributions from both the Golgi-apparatus and endoplasmic reticulum also help in the formation of ESEs [52,53]. The newly formed ESEs can merge with pre-existing ESEs inside the cells. Mature ESEs are called late-sorting endosomes (LSEs). In the process, they finally generate multivesicular bodies (MVBs) by inward budding of the endosomal limiting membrane. During this process, MVBs collect several intra-luminal vesicles (ILVs) [53,54]. These ILVs are also known as future exosomes. The

MVBs can degrade when they come in contact with lysosomes, but a fusion of MVBs with plasma membrane causes the release of exosomes. [55,56]

It is possible to characterize exosomes by determining their concentration and particle size distribution. The available techniques to measure the size and concentration are nanoparticle tracking analysis (NTA) [57], transmission electron microscopy (TEM) [58], a conventional flow cytometer, and resistive pulse sensing (RPS) [59]. None of these techniques accurately measure the size, concentration, and sample volume. The results obtained from these techniques differ by order of magnitude. This is because, in general, biological samples are a mixture of several components of different sizes, making them heterogeneous. [59] The most commonly used technique is the NTA, which combines light scattering microscopy and Brownian motion to achieve the particle size distribution of any liquid suspension [60]. NTA techniques can measure any particle in the liquid above about 70 nm [59].

3.2 Previous NMR studies

The study of exosomes has been ongoing for over two decades [61,62]. However, NMR studies of exosomes are scarce. Shao *et al.* reported circulating exosome detection using NMR [63]. They developed a microfluidic system for on-chip NMR (μ NMR) detection and quantification of exosome concentration. In this magnetic nano-sensor-based vesicle detection system, the exosomes were labeled with magnetic nanoparticles (MNPs) in order to detect circulating exosomes through T_2 contrast.

3.3 DOSY NMR analysis

In our studies, we extracted exosomes from three different sources: milk, embryonic kidney cells (EKC), and renal carcinoma cells (RCC). We made extractions from different batches and named them Milk 1-2, EKC 1-5, and RCC 1-4, respectively. After the extraction and purification, the samples were prepared for DOSY NMR experiments. Every exosome sample was prepared by adding 6 μ l of deuterium oxide (D_2O) into 30 μ l of a stock exosome solution. The concentrations of milk 2, EKC 3 and RCC 3 were 1.83×10^{11} , 1.04×10^{12} , and 2.54×10^{11} particles/ml, respectively. Then the whole volume was transferred into a 1.7 mm NMR tube. The DOSY NMR experiments were performed on a Bruker Avance 500 MHz spectrometer equipped with a micro cryoprobe at 280 K.

Figure 3.1a shows the 1H spectra of DOSY experiments of Milk, EKC, and RCC samples at the smallest gradient value. The peaks in the spectra at 0.9, 3.4, and 4.7 ppm arose from $-CH_3$, $-CH_2$ groups of ethanol and water, respectively. The ethanol signal arises from the residual ethanol used in the purification process. There were small signals in the region of 1.0-3.5 ppm, the most dominant between 1.8-2.0 ppm, which were assumed to originate from lipid $-CH_2$ groups. There was no peak visible in the aromatic region at around 7.0 ppm.

The DOSY decay curves of all three exosome samples for the most dominant signal at around 1.8-2.0 ppm are shown in Figure 3.1b. The decay rate for different samples is different because of different average particle size distributions. The EKC and RCC signals decay faster than the milk signal. This indicates that EKC and RCC have smaller particles

than milk. Inverse Laplace transform [25,64,65] analysis was used to convert decay curves into diffusion coefficient (D) distributions, shown in Figure 3.1c (Figure 3.1c is the sum of all diffusion distributions of different sample batches). There are multiple peaks in the diffusion coefficient distribution varying between 10^{-12} and 10^{-9} m^2/s . The smaller and larger values of diffusion coefficients represent larger complexes and small-sized particles, respectively. These diffusion coefficient values were then converted to size distributions (solid lines) shown in Figure 3.1d by using the Stokes-Einstein equation [66] and a comparison with nanoparticle tracking analysis distribution (dashed lines) was made. The Stokes-Einstein equation provides a reasonable approximation for spherical-shaped exosomes, which is larger than the solvent molecule (H_2O): [67–69]

$$D = \frac{kT}{6\pi\eta r_s} \quad (3.1)$$

Here, D is the diffusion coefficient, k is Boltzmann's constant, and η is the viscosity of the solvent. The intensities of the resulting particle size distributions of the DOSY NMR and NTA methods shown in Figure 3.1d are not directly comparable because the DOSY method represents the number of spins, while the NTA method represents the number of particles. The DOSY distribution detects particles in a broad range from a couple of nanometers close to a micrometer, while the NTA distribution detects particle sizes over 70 nm. In the

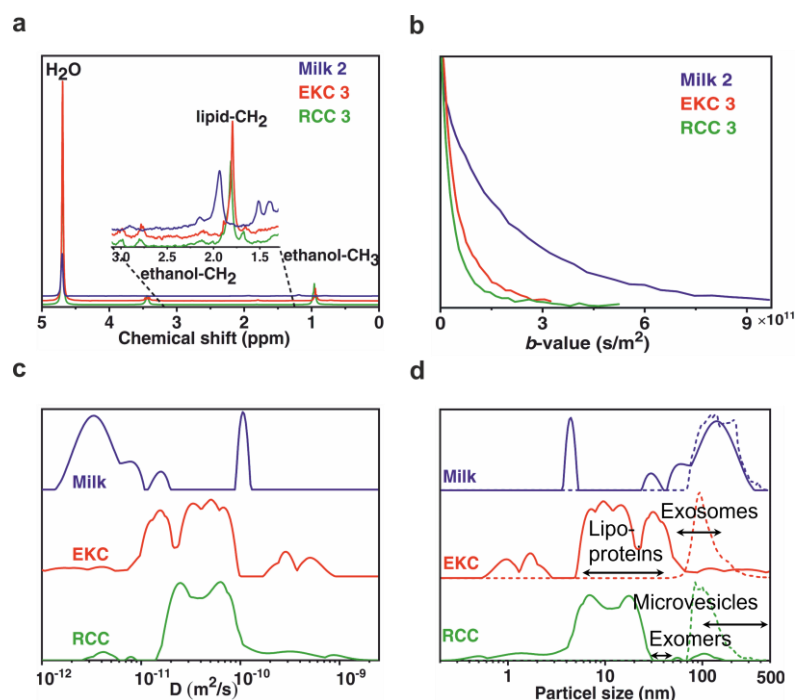


Figure 3.1. a) 1H DOSY spectra of selected Milk, EKC, and RCC exosome samples. All the spectra were recorded at the smallest gradient value. b) DOSY decay curves of the lipid CH_2 signals. c) Sum of diffusion coefficient distributions of all EV samples. d) Particle size distributions are derived from the diffusion coefficient distributions by the Stokes-

Einstein equation (solid lines) and corresponding NTA distributions (dashed lines). Reproduced from *Chem. Sci.* 12 (2021) 8311–8319 (CC BY-NC 3.0) [42].

DOSY distribution, a significant amount of small particles below 70 nm is invisible in the NTA. Exosomes are in the range of 50-150 nm; therefore, the broad size range indicates the presence of not only exosomes but also some other co-isolated particles together with exosomes such as lipoproteins (high-density lipoprotein (HDL), low-density lipoprotein (LDL) and intermediate-density lipoprotein (IDL), 5-35 nm), non-membranous exomers (30-50 nm), [70] and microvesicles (100-1000 nm) [45]. The DOSY and NTA distributions are in good qualitative agreement in the 70-400 nm range. The DOSY size distributions of the EKC and RCC samples are rather similar, whereas the milk distribution shows significantly larger particles.

3.3.1 Transmission electron microscopy analysis

The particle sizes were also estimated with transmission electron microscopy (TEM, Figure 3.2) to verify the results of the DOSY NMR analysis. The TEM images showed that the largest particles are 150–200 nm and aggregates are about 300 nm in diameter. There are

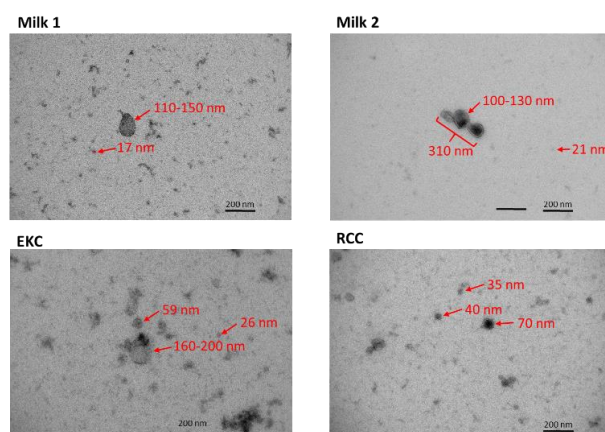


Figure 3.2. Transmission electron microscopy images with the estimated particle sizes of some milk, EKC, and RCC EV samples. Reproduced from *Chem. Sci.* 12 (2021) 8311–8319 (CC BY-NC 3.0) [42].

also many particles with sizes below 70 nm. This size range is below the detection limit of the NTA analysis but is observable in the DOSY analysis. In the milk sample, the images include small particles below 20 nm and large particles of 100-300 nm in diameter. Therefore, the TEM and the DOSY results are in good agreement. The EKC image shows a size distribution of a few to 200 nm, which also aligns with the DOSY analysis. The particle sizes visible in the RCC image are a bit smaller than the EKC particles present in the TEM image, which also agrees with the DOSY NMR results.

3.4 ^{129}Xe hyper-CEST NMR analysis

In hyper-CEST experiments, cryptophane-A mono-acid cages (CrA-ma) were first introduced into the sample to enhance the resolution. Xe gas was then bubbled into the EV sample through five capillary tubes. Figure 3.3b illustrates all the possible environments of Xe in the sample: free Xe in the sample solution, Xe temporarily trapped in the CrA-ma cages in solution, Xe trapped in cages in the lipid bilayer (exosomes) and encapsulated Xe in micelles.

The signal of encapsulated Xe in a CrA-ma cage in the lipid structure has a downfield shift of about 10 ppm from Xe in CrA-ma in an aqueous environment [71]. The hyper-CEST spectra of EKC at two different EV concentrations and RCC are shown in Figure 3.3a, which include signals at -124 ppm, -129 ppm, -134 ppm, and 0 ppm. The 0 ppm peak is an overlapping signal of the free xenon in the solvent and xenon in the lipid structure. When Xe is encapsulated in a CrA-ma cage, it provides well-resolved signals of different environments: signals in the range of -120 and -130 ppm correspond to Xe encapsulated in a CrA-ma cage in the lipid structures; the other signal at around -134 ppm originates from Xe encapsulated in a CrA-ma cage in the aqueous environment. In standard hyperpolarized ^{129}Xe spectra, the signals between -134 and -120 ppm were not visible. The significant signal enhancement provided by the CEST mechanism made them observable.

Two distinguished pools have 10 and 5 ppm downfield shifts from Xe in CrA-ma in the aqueous environment. These signals arise from lipid structures. We hypothesize that the signal at around -124 ppm represents larger nanoparticles such as exosomes and microvesicles. On the other hand, the other signal at around -129 ppm represents smaller nanosized particles, for example, lipoproteins and exomers. The results obtained from hyper-CEST confirm the existence of different subpopulations of extracellular nanoparticles observed in the DOSY analysis.

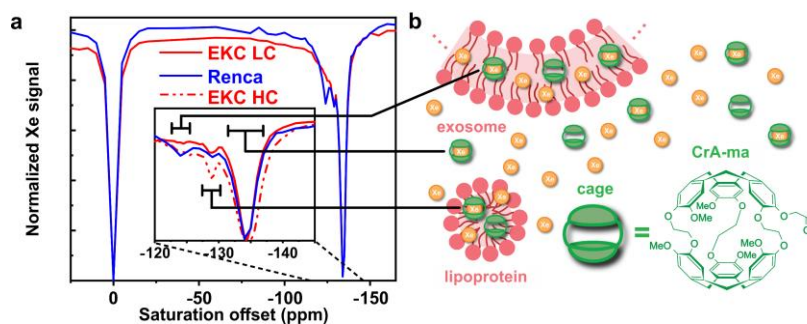


Figure 3.3. a) ^{129}Xe hyper-CEST spectra of EKC and RCC exosomes in PBS after labeling with a CrA-ma cage. The CEST responses from membrane-embedded CrA-ma cages are at ca. -125 and -130 ppm offset (relative to Xe in the buffer signal). Here, LC and HC indicate low and high concentration EV samples, respectively. b) All the components of the exosome sample in hyper-CEST experiments. Reproduced from *Chem. Sci.* 12 (2021) 8311–8319 (CC BY-NC 3.0) [42].

4. Ultrafast T_2 - T_2 study of ionic liquids

4.1 Ionic liquids

Ionic liquids (ILs) are mixtures of salts in a liquid state with several ions present; therefore, they show ionic conductivity. ILs have typical melting points below 100°C. ILs are typically organic salts or a mixture of organic and inorganic salts that melt or solidify at the same temperature.

Since the beginning to the present day, ILs have been categorized into first-generation, second-generation, and third-generation ILs. First-generation ILs were mostly used as solvents and catalysts of Friedel-Crafts reactions in organic chemistry and were able to interact with water. Therefore, they needed to be handled in a dry box. Second-generation ILs were also used extensively as solvents in organic chemistry and thought to be stable in water and in the presence of air. Afterward, it was shown that rising white fume and hydrolysis produced toxic and corrosive hydrogen fluoride. Third-generation ILs emerged in the early 2000s; they are chiral and task-specific [72]. ILs show various physical and chemical properties such as solvation, non-ionizing, low vapor pressure, thermal stability, nonflammability, ionic conductivity, and low volatility. These properties make ILs a lucrative candidate for scientific and technological applications such as catalysis, organic synthesis, active pharmaceutical ingredients, biopolymer processing, nuclear fuel processing, waste recycling, solar thermal energy storage, and much more. [72,73]

Having all the advantages of ILs, they are still not used in many industrial applications due to halogen-containing anions (HF_6^- , BF_4^-). Due to hydrolysis, these halogens containing ILs tend to absorb water and produce hydrogen halides and other acidic byproducts. The reaction byproducts exhibit environmental issues, toxicity, and are corrosive in nature. Therefore, ILs are not always considered to be green [74,75]. Recent studies have shown that halogen-free ILs mitigate toxicity and corrosion issues. Environmentally friendly halogen-free orthoborate-based hydrophobic ILs are used, e.g., as lubricants. [76,77]

4.2 Relaxation and diffusion NMR studies of ionic liquids

NMR relaxation and diffusion experiments offer a better understanding of physicochemical properties, aggregations, hydrogen bonding, and solvation dynamics at the atomic level [78]. There are plenty of NMR studies conducted on ILs. For example, Filippov *et al.* [79] reported the self-diffusion coefficient of an IL and explained the coexisting of two liquid phases depending on the temperature. Javed *et al.* [79,80] recently studied the same IL by combining 1D and multidimensional LNMR methods. The study showed that the microscopic phase structures and the chemical shifts change as a function of temperature. Endo *et al.* [81] conducted a relaxation NMR study on an IL and reported that mostly stable anion interaction sites play a significant part in the rotational dynamics of IL.

In the current study (Paper 2), a new ultrafast T_2 - T_2 relaxation exchange pulse sequence was introduced, and its feasibility was demonstrated by following the molecular exchange of an IL system. The method used in the experiments is ultra-efficient in terms of time-saving and provides high-resolution data. As the method allows measurement of T_2 - T_2 data in a single scan, it provides significant time-saving and facilitates the use of hyperpolarization to boost the experimental sensitivity.

4.3. Method

The UF T_2 - T_2 exchange sequence is shown in Figure 4.1. Its conventional counterpart is introduced in Section 2.6.

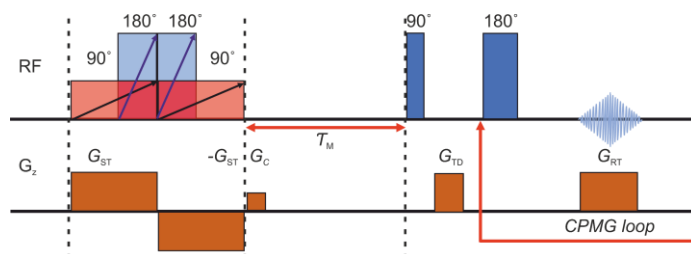


Figure 4.1. UF T_2 - T_2 exchange pulse sequence.

The UF T_2 - T_2 pulse sequence contains two transverse relaxation encoding parts which are highlighted by the dashed lines. These parts are separated by a mixing period (τ_M). The first part consists of partially overlapping 90° and 180° adiabatic frequency-swept pulses forming a double spin echo, and simultaneous gradient pulses. The frequency of the frequency-swept pulses increases linearly with time. The simultaneous gradient pulses make the magnetic field linearly dependent on the position, hence making the Larmor frequency of the nucleus position-dependent. Consequently, the double spin echo time becomes zero and maximum at the top and bottom of the sample, respectively. If the gradient amplitude is low, the signal decay is dominated by T_2 relaxation. The data is read in a single-scan fashion via the application of the CPMG loop along with the gradients. The gradients are needed for reading the spatially encoded data. Then the collected data

are analyzed with ILT based on the Iterative Thresholding Algorithm for Multiexponential Decay (ITAMeD) [82] to extract the 2D relaxation time distribution.

In the first spatial encoding block, the overall double spin-echo time (t_1) as a function of position (z) is

$$t_1(z) = 2 \left(1 - \frac{\gamma G_S z}{\pi \Delta \nu} \right) t_F^{90^\circ}, \text{ when } -\frac{\pi \Delta \nu}{\gamma G_S} \leq z \leq \frac{\pi \Delta \nu}{\gamma G_S}. \quad (4.1)$$

Here, $t_F^{90^\circ}$ is the 90° chirp pulse duration, and G_S is the first spatial encoding gradient amplitude, γ is the gyromagnetic ratio, and $\Delta \nu$ is the sweep width. The echo amplitude in the first spatial encoding block is

$$E_1(z) = E_1^0 \exp \left[- \left(R_{21} + \frac{\gamma^2 G_S^2 [t_1(z)]^2}{48} D_1 \right) t_1(z) \right], \quad (4.2)$$

where E_1^0 is the initial signal amplitude, R_{21} is the transverse relaxation rate in the first spatial encoding block, and D_1 is the diffusion coefficient during the first spatial encoding block. The former and latter terms in the parenthesis govern the signal decay due to the T_2 relaxation and diffusion, respectively. In the case of the IL study, the latter term is negligible and can be discarded in this case due to the slow diffusion of the ions.

The echo amplitude in the CPMG block is

$$E_2(t_2) = E_0^2 \exp \left[- \left(R_{22} + \frac{\gamma^2 G_{\text{Reff}}^2 \tau^2}{3} D_2 \right) t_2 \right], \quad (4.3)$$

where, R_{22} is the transverse relaxation rate, G_{Reff} is the gradient pulse amplitude with the length of τ and the area corresponds to the area of the read gradient, G_R . The time between 90° and 180° pulses is τ . D_2 is the diffusion coefficient and t_2 is the time variable in the second dimension. The second term in the parenthesis reflects the diffusion decay, which is negligible in this case and can be discarded. After discarding both diffusion decay terms in Eqs. (4.2) and (4.3), the overall signal becomes

$$E[t_1(z), t_2] = E_0 \int P(R_{21}, R_{22}) \exp[R_{21} t_1(z)] \exp[R_{22} t_2] dR_{21} dR_{22}. \quad (4.4)$$

4.4 Results

The ^1H NMR spectrum (Figure 4.2) shows the presence of cation and anion signals in the IL sample at around 0-2 ppm and 6-8 ppm, respectively.

The UF T_2 - T_2 experiments data were processed using ITAMeD [82] for 2D ILT to obtain the 2D maps (Figures 4.3b-c). In the ILT, only the highlighted area of raw data (Figure 4.3a) covering the spatial encoding region without the edges affected by CHIRP imperfections was used.

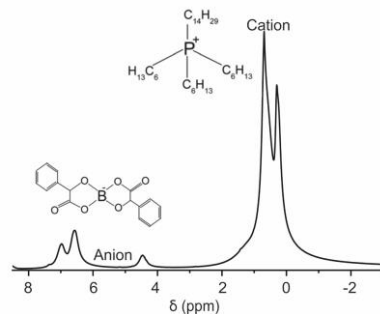


Figure 4.2. ^1H spectrum of trihexyl(tetradecyl)phosphonium, $[\text{P}_{6,6,6,14}]^+$, cation and bis(mandelato)borate, $[\text{BMB}]^-$, anion of the ionic liquid measured at room temperature.

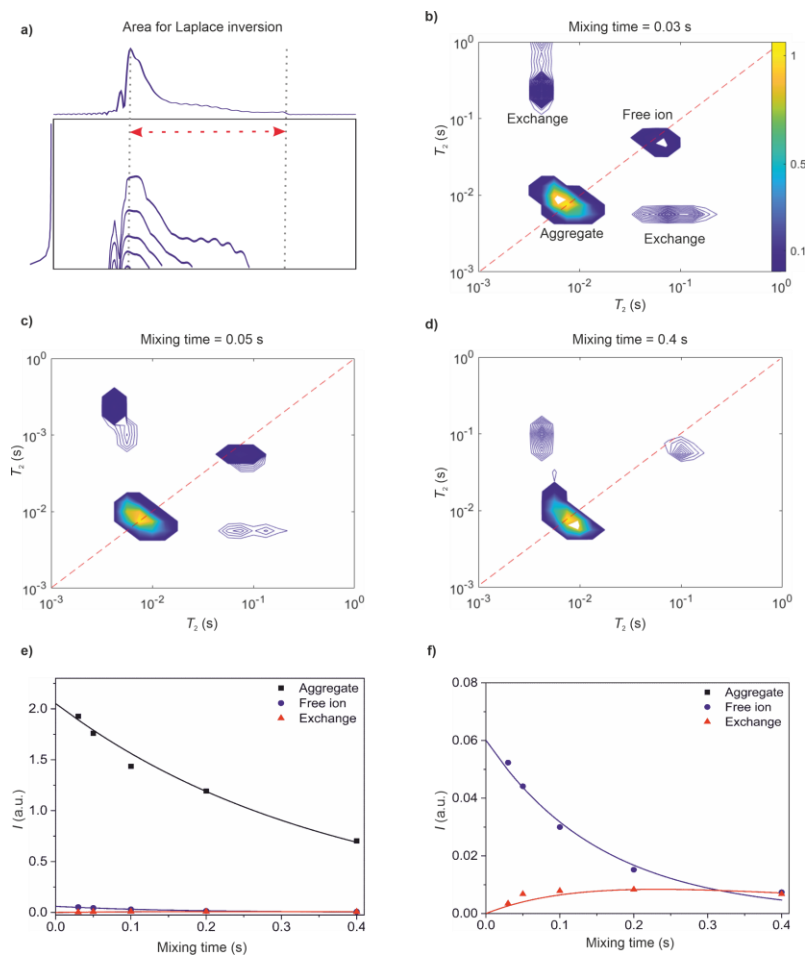


Figure 4.3. UF T_2 - T_2 exchange experiments of the ionic liquid sample. a) The raw data was collected at 30 ms mixing period, and the area indicated by the gray and red dashed

line was used in the Laplace inversion. The 2D maps at b) 30, c) 50, and d) 400 ms mixing periods were obtained from 2D ILT. e) The two-site exchange model fitted with the integral values of the peaks as a function of mixing time (τ_M). f) Zoom-in of e). The asymmetry in the cross peaks in the distributions is expected to arise from noise.

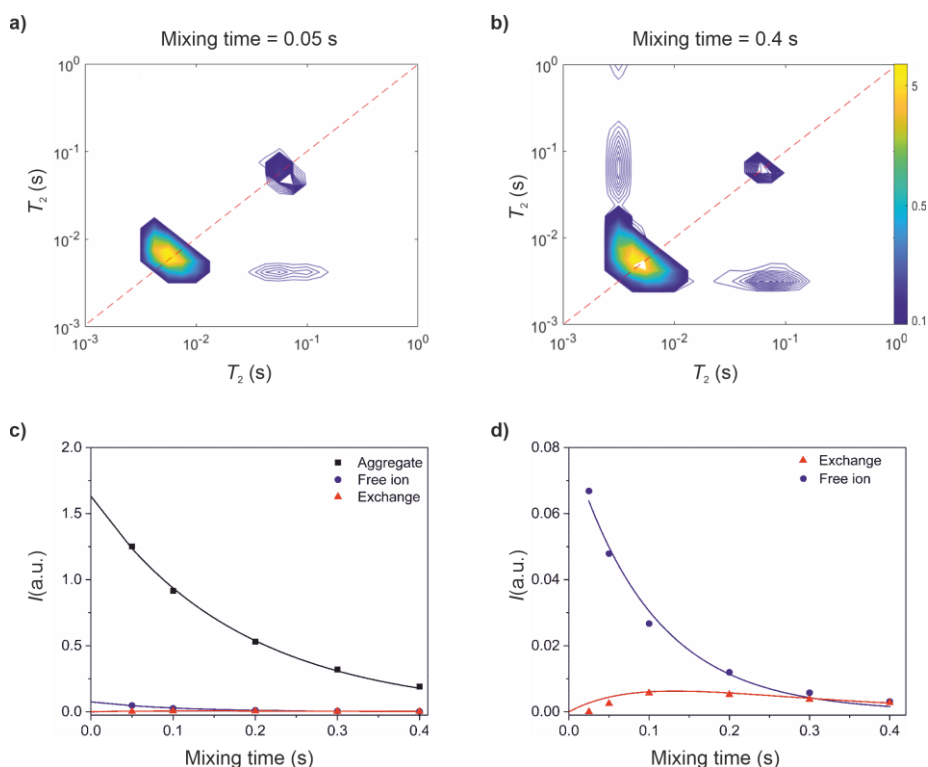


Figure 4.4. Conventional T_2 - T_2 analysis of the IL sample. T_2 - T_2 exchange maps resulting from a 2D inverse Laplace transform of the raw data measured with mixing times of a) 50 and b) 400 ms. c) Integrals of the T_2 - T_2 peaks as a function of mixing time. The solid lines represent a fit of a two-site exchange model. d) Zoom-in area of c).

The 2D maps include two diagonal peaks in the maps. The aggregates and the free ions have T_2 of 10 and 86 ms, respectively. The exchange between the aggregates and free ions is evident from the cross-peaks. The intensity of the cross-peaks varies depending on the mixing time; in the beginning, the intensity increases, and later it reaches the plateau.

From the 2D ILT maps, the integral values of the diagonal peaks and cross-peaks (Figures 4.3b-d) were collected to determine the molecular exchange rates by fitting a two-site exchange model into the integral values (Figures 4.3e and 4.3f) [18]. The exchange rates ($k = 1.7 \pm 1.1 \text{ s}^{-1}$, $k_{AB} = 0.04 \pm 0.03 \text{ s}^{-1}$ and $k_{BA} = 1.7 \pm 1.1 \text{ s}^{-1}$) obtained from the UF experiments are in good agreement with reference measurements (Figures 4.4a-d) ($k = 1.8 \pm 0.9 \text{ s}^{-1}$, $k_{AB} = 0.08 \pm 0.04 \text{ s}^{-1}$ and $k_{BA} = 1.8 \pm 0.9 \text{ s}^{-1}$).

One conventional T_2 - T_2 exchange experiment with 8 scans and a 3 s relaxation delay took 8 hours [80]. A set of conventional T_2 - T_2 exchange experiments with 5 different

mixing times took 40 hours. Whereas one UF T_2 - T_2 exchange experiment with a 7 s relaxation delay and 512 scans took only 1 hour and a set of experiments with five different mixing times took only 5 hours. Therefore, the UF experiments are more than an order of magnitude faster even with a long relaxation delay compared to its conventional counterpart. One UF T_2 - T_2 exchange experiment with a 3 s relaxation delay and 512 scans would take only 28 minutes. The efficient UF T_2 - T_2 method would enable studying porous media [83] as well as the characterization of a biological sample, for example, exosomes [42] with insignificant sample evolution. The UF method has many potential applications in biochemistry, chemistry, and medicine. The pulse sequence shown in Figure 4.1 can also be used for UF diffusion exchange spectroscopy (DEXSY) experiments if stronger gradients are used and signal decay is dominated by diffusion instead of T_2 relaxation (see Eqs. 4.2 and 4.3).

5. Nonlinear sampling in ultrafast Laplace NMR

5.1 Nonlinear sampling

In the LNMR experiment, sampling in any dimension can be done linearly or nonlinearly. The exponentially time-dependent data is sampled with a constant time step in linear sampling. As a result, the data, in the beginning, is non-optimal since most of the rapid changes occur in this part. If the data consists of more than one exponential component, it becomes worse because in most cases, the rapidly changing component may not be sampled at all. In nonlinear sampling, the data is collected logarithmically, *i.e.*, by keeping the difference of natural logarithms of successive sampling point times constant. Therefore, the initial part of the data is heavily sampled, resulting in optimal data detection for single or multi-exponential components [84]. Thus, nonlinear sampling provides a more optimal way for data collection.

5.2 Method

In UF-LNMR experiments, the spatial encoding part consists of adiabatic frequency-swept and gradient pulses. The frequency of the adiabatic pulse changes linearly with time. As a result, the sampling of the indirect dimension becomes linear (non-optimal) [30,85–90].

Let us consider the UF T_1 - T_2 correlation experiment (Figure 5.1a) as an example. The spatial encoding part of the pulse sequence consists of a frequency-swept π pulse and a gradient pulse G_{se} . In this case, the frequency of the frequency-swept pulse decreases with time, and the gradient pulse makes the Larmor frequency linearly dependent on the position.

The simultaneous application of a frequency-swept and gradient pulse inverts the spins at the top first and those at the bottom last (Figure 5.1b). The inversion time depends linearly on the position of the spins. During the initial pulses, the spins inverted at the beginning of the pulse recover almost back to the thermal equilibrium and ones inverted at

the end of the pulse recover hardly at all. In between the recovery is linearly dependent on the position and therefore results in the magnetization profile shown in the last column of Figure 5.1b. The magnetization profile along the z-axis is identical to the standard inversion recovery curve with linear time step. Then, data is read using the CPMG loop and read gradients.

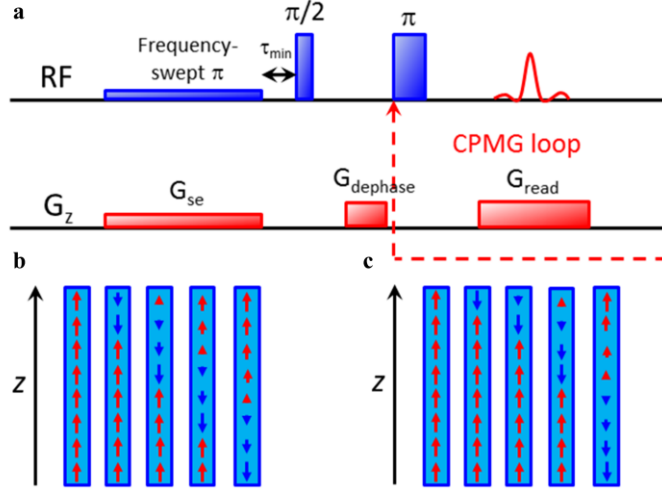


Figure 5.1. a) Ultrafast T_1 - T_2 correlation pulse sequence. The magnetization vectors in the different layers of the sample in the case of b) linear and c) nonlinear frequency sweep used during spatial encoding, respectively. Reproduced from *J. Magn. Reson.* 307 (2019): 106571 (CC BY 4.0) [91].

If the frequency sweep of the frequency-swept π pulse is nonlinear, then the sampling of the indirect dimension of the UF T_1 - T_2 experiment changes from linear to logarithmic sampling. For logarithmic sampling, the frequency of the adiabatic pulse, ν_F , must change logarithmically with time t :

$$\nu_F = \Delta\nu \left[\frac{\ln \left[\frac{1}{2}(\tau_{\max} + \tau_{\min}) - (\tau_{\max} - \tau_{\min}) \frac{t}{t_F} \right] - \ln(\tau_{\max})}{\ln(\tau_{\max}) - \ln(\tau_{\min})} + \frac{1}{2} \right]. \quad (5.1)$$

Here, $\Delta\nu = \nu_i - \nu_f$ is the frequency sweep width, ν_i and ν_f are the initial and final frequencies of the sweep, respectively, τ_{\min} is the minimum recovery time, and τ_{\max} is the maximum recovery time (Figure 5.1a). The length of the π frequency-swept pulse is $t_F = \tau_{\min} - \tau_{\max}$, and $-\frac{t_F}{2} \leq t \leq +\frac{t_F}{2}$. The recovery time τ increases exponentially with the position z according to the following equation:

$$\tau = \exp \left\{ [\ln(\tau_{max}) - \ln(\tau_{min})] \left(\frac{\gamma G z}{2\pi\Delta\nu} - \frac{1}{2} \right) + \ln(\tau_{max}) \right\}. \quad (5.2)$$

Here, γ and G are the gyromagnetic ratio and gradient strength, respectively, and $-\pi\Delta\nu/\gamma G \leq z \leq +\pi\Delta\nu/\gamma G$ is the spatial encoding region.

5.3 Results

The samples used in the experiment included 2% H₂O in D₂O. For the single-tube sample, a 0.046 M solution of CuCl₂×2H₂O was added to a 5 mm NMR tube. The double-tube system was made by placing a 3 mm NMR tube into a 5 mm NMR tube. In the double-tube system, inside and outside the 3 mm NMR tube, a CuCl₂×2H₂O solution of 0.0046 M and 0.046 M was added, respectively.

Another sample of Silica gel 60 (purchased from Merck, Darmstadt, Germany) was also examined in this study. The sample was prepared by impregnating silica gel 60 with 0.0046 M of CuCl₂×2H₂O solution. After that, the sample was immersed with an excess of water (2% H₂O in D₂O) in a 5 mm NMR tube. All the measurements for this study were carried out on a Bruker Avance III 400 MHz spectrometer at room temperature. The spectrometer was equipped with a standard 5 mm BBO probe.

The nonlinear sampling method was tested on a single- and double-tube water sample (Figure 5.2a) using UF inversion recovery (UF IR) measurements. The experiment is otherwise identical to the UF T_1 - T_2 experiment shown in Figure 5.1a, but only one echo was collected in the CPMG loop. Here, we will only discuss the results of the double-tube measurement, and the single-tube results are available in Paper 3 [91]. According to the reference measurement, T_1 in the inner compartment of the double-tube sample was about 10 times longer (332 ± 2 ms) than the outer compartment (33.5 ± 0.2 ms). In the spatial encoding, the frequency of the frequency-swept π pulse increased nonlinearly from -5000 to $+5000$ Hz (Figure 5.2b), and the pulse length t_F was 1 s. To compare results of linear and nonlinear sampling, both linear and nonlinear frequency sweeps were used (Figure 5.2b).

The magnetization profile observed in the nonlinearly sampled UF IR experiment is shown in Figure 5.2c (red curve). The IR curve has two minima at around $z = -2$ and -4 mm. The one at about $z = -2$ mm corresponds to the zero intensity of the IR curve. The other one at about $z = -4$ mm is an artefact and arises from the fact that the adiabatic pulses do not work perfectly at the beginning and the end [90]. In the case of nonlinear sampling, the IR curve seems to be better probed as compared to that for the linear sampling (Figure 5.2c, blue dashed curve).

The UF-IR curves extracted from the magnetization profiles are shown in Figure 5.2d. As the adiabatic pulse does not work perfectly at the beginning and end of the frequency sweep, the data from that region were neglected [85]. The position axis z was then converted into the recovery time axis τ . The IR curve of the nonlinearly sampled data seems more optimally sampled (red curve), especially for the shorter recovery times in the beginning than the linearly sampled curve (blue dashed curve). The recovery time range probed by linear sampling was from 102 to 910 ms, and from 18 to 747 ms for nonlinear

sampling. The T_1 values obtained from exponential fits are in better agreement with the reference values in the case of nonlinear sampling.

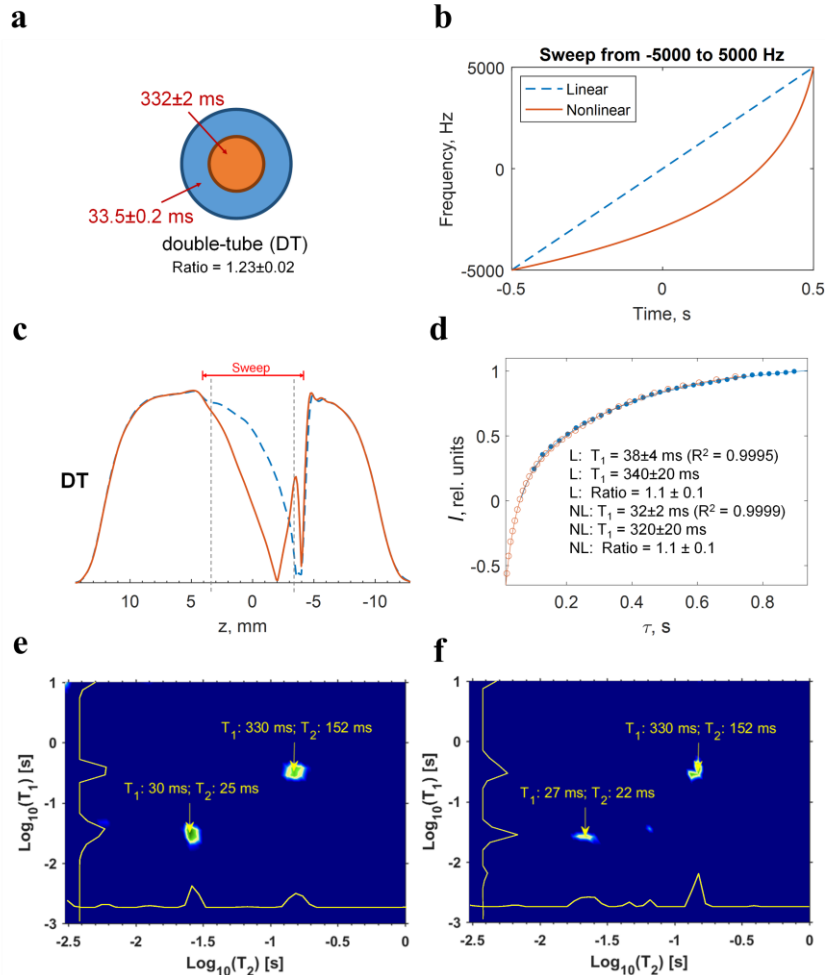


Figure 5.2. a) Illustration of a double-tube water sample. Relaxation times (shown in the figure) were made different in the compartments by doping with copper chloride. b) The frequency sweeps used in the linearly and nonlinearly sampled experiments. c) Magnetization profile detected in the UF experiment; the vertical gray dotted lines indicate the area used in the T_1 data analysis. d) Inversion recovery curves and least square fits of UF T_1 - T_2 maps measured with e) linear and f) nonlinear sampling, respectively. The minor peaks visible in the T_1 - T_2 distributions are artefacts due to experimental noise. Adapted from *J. Magn. Reson.* 307 (2019): 106571 (CC BY 4.0) [91].

T_1 - T_2 maps measured by linearly and nonlinearly sampled UF T_1 - T_2 experiments are shown in Figures 5.2e and 5.2f. They include two signals corresponding to the inner and outer compartments. The maps are in good agreement. However, the signals are about 40%

narrower in the T_1 direction in the nonlinearly sampled experiments, indicating improved resolution.

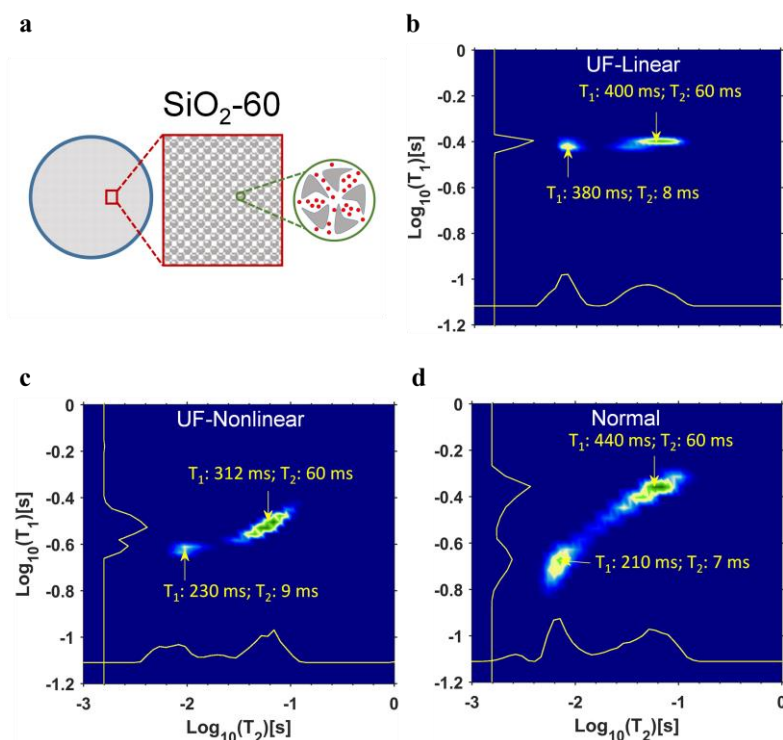


Figure 5.3. a) Illustration of impregnated silica gel 60 in $\text{CuCl}_2 \times 2\text{H}_2\text{O}$ solution. UF T_1 - T_2 correlation maps were measured using b) linear and c) nonlinear sampling. d) The reference map. Adapted from *J. Magn. Reson.* 307 (2019): 106571 (CC BY 4.0). [91]

As another proof of principle, we ran the measurements with Silica gel 60. An illustration of the sample can be found in Figure 5.3a. Linearly, nonlinearly sampled UF and conventional T_1 - T_2 correlation maps are shown in Figures 5.3b, c, and d, respectively. There are two peaks visible in the 2D maps; one arises from the water inside the pores (nominal pore size 60 Å) and corresponds to shorter relaxation times, and the other one arises from the bulk water presented in between the Silica gel 60 particles (particle size 63–200 μm). In the T_1 dimension, the linearly sampled UF map signals are in a significantly narrower region than in the nonlinearly sampled map because of non-optimal sampling. On the hand, the signals in the nonlinearly sampled UF 2D maps are in a slightly narrower area as compared to its standard reference map. This may be a consequence of the effect of magnetic field inhomogeneity in the porous sample on spatial encoding. However, the presence of two water sites, average T_1 values, and the T_2 ranges of the UF data align with the standard reference data map. We may consider the peak width as an experimental error; within the peak widths, the maps and top coordinates of the peaks of the UF nonlinear data and standard reference data are in good agreement.

Notably, the UF experiments are more time-efficient than their conventional counterparts. In this case, in UF experiments it took only 30 s to acquire four scans, whereas the reference experiment required 16 minutes to obtain the same number of scans. In UF experiments, the samples are split into several layers in spatial encoding, leading to a decrease in the signal-to-noise ratio (SNR) compared to the standard reference experiments. In the UF experiments, the drop in the observed SNR is relatively small. However, this can be fixed by repeating the UF experiment several times within the time frame of a single traditional experiment, which increases the SNR [86,88]. Additionally, the UF experiment offers a single-scan approach; therefore, the use of hyperpolarization make it feasible to increase the sensitivity of the UF experiments by several orders of magnitude. [30,86,87,92]

6. Summary and conclusions

The present thesis focuses on the characterization of nanosized vesicles and the development and application of ultrafast experiments. Traditional multidimensional NMR experiments are time-consuming, and this problem has been tackled with the utilization of spatial encoding of the data into different layers of the sample, which facilitates the acquisition of multidimensional experimental data in a single scan.

In Paper 1, advanced NMR methods, namely ^1H DOSY NMR and ^{129}Xe hyper-CEST were used to study exosomes. The DOSY NMR was used to characterize and estimate exosomes of different sources based on sizes, and the hyper-CEST was used to distinguish different environments in the sample with higher sensitivity and specificity. The analysis reveals vesicles of various sizes, even if the size is below the detection limit of the standard nanoparticle tracking analysis. The duration of the DOSY NMR experiment was very long, about 50 hours. More efficient LNMR techniques, such as single-scan CPMG experiments, could be used to reduce the experiment time. The SNR could be improved by using a higher magnetic field and a larger amount of concentrated sample.

In Paper 2, a novel ultrafast 2D T_2 - T_2 exchange experiment (UF REXSY) was introduced, and its feasibility was demonstrated by studying the aggregation ions in an ionic liquid and quantifying the molecular exchange rate efficiently. This single-shot experiment can also be used in ultrafast diffusion exchange spectroscopy (UF DEXSY) with minor modifications. [93]

Paper 3 demonstrates the feasibility of using nonlinear instead of traditional linear sampling in the indirect dimension of the UF inversion recovery (UF IR) and T_1 - T_2 correlation experiments. Like its linearly sampled counterpart, this method is based on the use of frequency swept pulses, but with a nonlinear frequency sweep. Nonlinear sampling results in a more optimal sampling of the data with enhanced resolution and can be used in other multidimensional NMR experiments to optimize data sampling.

To conclude, this thesis complements the NMR toolbox with a couple of efficient techniques that facilitate studying biological samples (exosomes) [42], ionic liquids [94] and porous materials (silica gel) [91]. The NMR techniques developed also offer promising prospects for a wide range of other applications in chemistry, biochemistry, and material

science. In principle, ultrafast LNMR experiments require a homogeneous sample region for spatial encoding. However, small inhomogeneities can be compensated in postprocessing by using 1D MRI data. The methods used in this thesis are also feasible with affordable, low-field mobile NMR devices [88,92] for conducting different analyses time-efficiently outside of the laboratory environment with higher sensitivity, using hyperpolarization.

References

- [1] E. M. Purcell, H. C. Torrey, and R. V. Pound, *Phys. Rev.* **69**, 37 (1946).
- [2] F. Bloch, W. W. Hansen, and M. Packard, *Phys. Rev.* **69**, 127 (1946).
- [3] E. J. Fordham, L. Venkataramanan, J. Mitchell, and A. Valori, *Diffus. Fundam.* **29**, 2 (2017).
- [4] L. Frydman, T. Scherf, and A. Lupulescu, *Proc. Natl. Acad. Sci.* **99**, 15858 (2002).
- [5] P. Pelupessy, *J. Am. Chem. Soc.* **125**, 12345 (2003).
- [6] P. Giraudeau and L. Frydman, *Annu. Rev. Anal. Chem. (Palo Alto, Calif.)* **7**, 129 (2014).
- [7] V.-V. Telkki, M. Urbańczyk, and V. Zhivonitko, *Prog. Nucl. Magn. Reson. Spectrosc.* **126–127**, 101 (2021).
- [8] A. Abragam, *The Principles of Nuclear Magnetism* (Oxford university press, 1961).
- [9] M. H. Levitt, *Spin Dynamics: Basics of Nuclear Magnetic Resonance* (John Wiley & Sons, 2013).
- [10] J. Keeler, *Understanding NMR Spectroscopy*, Second Edition (John Wiley & Sons, 2007).
- [11] H. Friebolin, *Basic One-and Two-Dimensional NMR Spectroscopy* (Wiley, 2005).
- [12] E. L. Hahn, *Phys. Rev.* **76**, 145 (1949).
- [13] W. Kittler, M. Hunter, and P. Galvosas, *Phys. Rev. E. Stat. Nonlinear, Soft Matter Phys.* **92**, 023016 (2015).
- [14] E. L. Hahn, *Phys. Rev.* **80**, 580 (1950).

- [15] S. Meiboom and D. Gill, *Rev. Sci. Instrum.* **29**, 688 (2004).
- [16] E. O. Stejskal and J. E. Tanner, *J. Chem. Phys.* **42**, 288 (1965).
- [17] J. E. Tanner, *J. Chem. Phys.* **52**, 2523 (1970).
- [18] J. Jeener, B. H. Meier, P. Bachmann, and R. R. Ernst, *J. Chem. Phys.* **71**, 4546 (1979).
- [19] P. T. Callaghan, *Translational Dynamics and Magnetic Resonance : Principles of Pulsed Gradient Spin Echo NMR* (Oxford University Press, 2011).
- [20] J. Kowalewski and L. Mäler, *Nuclear Spin Relaxation in Liquids: Theory, Experiments, and Applications, Second Edition* (CRC Press, 2017).
- [21] Y. Q. Song, *J. Magn. Reson.* **229**, 12 (2013).
- [22] S. W. Provencher, *Comput. Phys. Commun.* **27**, 229 (1982).
- [23] G. C. Borgia, R. J. S. Brown, and P. Fantazzini, *J. Magn. Reson.* **132**, 65 (1998).
- [24] D. Bernin and D. Topgaard, *Curr. Opin. Colloid Interface Sci.* **18**, 166 (2013).
- [25] Y. Q. Song, L. Venkataramanan, M. D. Hürlimann, M. Flaum, P. Frulla, and C. Straley, *J. Magn. Reson.* **154**, 261 (2002).
- [26] V.-V. Telkki, *Magn. Reson. Chem.* **56**, 619 (2018).
- [27] Y. Qiao, P. Galvosas, T. Adalsteinsson, M. Schönhoff, and P. T. Callaghan, *J. Chem. Phys.* **122**, 214912 (2005).
- [28] M. D. Hürlimann and L. Venkataramanan, *J. Magn. Reson.* **157**, 31 (2002).
- [29] V.-V. Telkki and V. V. Zhivonitko, in *Annual Reports on NMR Spectroscopy*, Vol. 97 (Academic Press, 2019), pp. 83–119.
- [30] O. Mankinen, J. Hollenbach, S. Ahola, J. Matysik, and V.-V. Telkki, *Microporous Mesoporous Mater.* **269**, 75 (2018).
- [31] M. Urbańczyk, Y. Kharbanda, O. Mankinen, and V.-V. Telkki, *Anal. Chem.* **92**, 9948 (2020).
- [32] C. Leon Swisher, B. Koelsch, S. Sukumar, R. Sriram, R. D. Santos, Z. J. Wang, J. Kurhanewicz, D. Vigneron, and P. Larson, *J. Magn. Reson.* **257**, 102 (2015).
- [33] A. Tannús and M. Garwood, *NMR Biomed* **10**, 423 (1997).
- [34] B. Blumich, *NMR Imaging of Materials*, Vol. 57 (OUP Oxford, 2000).
- [35] B. Blümich, *Low-Field and Unilateral NMR* (Springer, 2005).
- [36] K. Bartik, P. Choquet, A. Constantinesco, G. Duhamel, J. Fraissard, J.-N. Hyacinthe, J. Jokisaari, E. Locci, T. J. Lowery, M. Luhmer, and others, *Actual.*

- Chim **287**, 16 (2005).
- [37] M. M. Spence, E. J. Ruiz, S. M. Rubin, T. J. Lowery, N. Winssinger, P. G. Schultz, D. E. Wemmer, and A. Pines, *J. Am. Chem. Soc.* **126**, 15287 (2004).
- [38] L. Schröder, *Phys. Medica* **29**, 3 (2013).
- [39] L. D. Kispert, L. S. Cooray, S. K. Wu, Prepr, Pap, J. S. Gethner, R. E. Winans, P. Thiagarajan, and R. B. Stephens, *Energy and Fuels* **5**, 87 (1991).
- [40] V. V. Terskikh, I. L. Moudrakovski, S. R. Breeze, S. Lang, C. I. Ratcliffe, J. A. Ripmeester, and A. Sayari, *Langmuir* **18**, 5653 (2002).
- [41] J. Demarquay and J. Fraissard, *Chem. Phys. Lett.* **136**, 314 (1987).
- [42] M. S. Ullah, V. V. Zhivonitko, A. Samoylenko, A. Zhyvolozhnyi, S. Viitala, S. Kankaanpää, S. Komulainen, L. Schröder, S. J. Vainio, and V.-V. Telkki, *Chem. Sci.* **12**, 8311 (2021).
- [43] T. G. Walker and W. Happer, *Rev. Mod. Phys.* **69**, 629 (1997).
- [44] M. Record, S. Silvente-Poirot, M. Poirot, and M. O. Wakelam, *J. Lipid Res.* **59**, 1316 (2018).
- [45] M. Mathieu, L. Martin-Jaular, G. Lavieu, and C. Théry, *Nat. Cell Biol.* **21**, 9 (2019).
- [46] H. Valadi, K. Ekström, A. Bossios, M. Sjöstrand, J. J. Lee, and J. O. Lötvall, *Nat. Cell Biol.* **9**, 654 (2007).
- [47] J. Naureen and M. Debabrata, *J. Biomed. Res.* **31**, 386 (2017).
- [48] K. Laulagnier, C. Motta, S. Hamdi, S. Roy, F. Fauvelle, J. F. Pageaux, T. Kobayashi, J. P. Salles, B. Perret, C. Bonnerot, and M. Record, *Biochem. J.* **380**, 161 (2004).
- [49] M. H. Rashed, E. Bayraktar, G. K. Helal, M. Abd-Ellah, P. Amero, A. Chavez-Reyes, and C. Rodriguez-Aguayo, *Int. J. Mol. Sci.* **18**, 538 (2017).
- [50] J. S. Schorey and S. Bhatnagar, *Traffic* **9**, 871 (2008).
- [51] S. Gurunathan, M.-H. Kang, M. Jeyaraj, M. Qasim, and J.-H. Kim, *Cells* **8**, 307 (2019).
- [52] E. Willms, C. Cabañas, I. Mäger, M. J. A. Wood, and P. Vader, *Front. Immunol.* **9**, 738 (2018).
- [53] N. P. Hessvik and A. Llorente, *Cell. Mol. Life Sci.* **75**, 193 (2018).
- [54] E. Cocucci and J. Meldolesi, *Trends Cell Biol.* **25**, 364 (2015).
- [55] M. Record, *Placenta* **35**, 297 (2014).

- [56] R. Sahu, S. Kaushik, C. C. Clement, E. S. Cannizzo, B. Scharf, A. Follenzi, I. Potolicchio, E. Nieves, A. M. Cuervo, and L. Santambrogio, *Dev. Cell* **20**, 131 (2011).
- [57] C. Y. Soo, Y. Song, Y. Zheng, E. C. Campbell, A. C. Riches, F. Gunn-Moore, and S. J. Powis, *Immunology* **136**, 192 (2012).
- [58] V. Goertz, N. Dingenouts, and H. Nirschl, *Part. Part. Syst. Charact.* **26**, 17 (2009).
- [59] E. van der Pol, F. A. W. Coumans, A. E. Grootemaat, C. Gardiner, I. L. Sargent, P. Harrison, A. Sturk, T. G. van Leeuwen, and R. Nieuwland, *J. Thromb. Haemost.* **12**, 1182 (2014).
- [60] B. Vestad, A. Llorente, A. Neurauder, S. Phuyal, B. Kierulf, P. Kierulf, T. Skotland, K. Sandvig, K. B. F. Haug, and R. Øvstebø, *J. Extracell. Vesicles* **6**, 1344087 (2017).
- [61] S. T. Y. Chuo, J. C. Y. Chien, and C. P. K. Lai, *J. Biomed. Sci.* **25**, 1 (2018).
- [62] J. L. Hood, *Nanomedicine* **11**, 1745 (2016).
- [63] H. Shao, J. Chung, L. Balaj, A. Charest, D. D. Bigner, B. S. Carter, F. H. Hochberg, X. O. Breakefield, R. Weissleder, and H. Lee, *Nat. Med.* **18**, 1835 (2012).
- [64] P. D. Teal and C. Eccles, *Inverse Probl.* **31**, 045010 (2015).
- [65] L. Venkataramanan, Y. Q. Song, and M. D. Hürlimann, *IEEE Trans. Signal Process.* **50**, 1017 (2002).
- [66] Albert Einstein, *Ann. Phys.* **322**, 549 (1905).
- [67] P. Dvořák, M. Šoltésová, and J. Lang, *Mol. Phys.* **117**, 868 (2018).
- [68] R. Neufeld and D. Stalke, *Chem. Sci.* **6**, 3354 (2015).
- [69] R. Evans, Z. Deng, A. K. Rogerson, A. S. McLachlan, J. J. Richards, M. Nilsson, G. A. Morris, R. Evans, Z. Deng, A. K. Rogerson, M. Nilsson, G. A. Morris, A. S. McLachlan, and J. J. Richards, *Angew. Chemie Int. Ed.* **52**, 3199 (2013).
- [70] H. Zhang, D. Freitas, H. S. Kim, K. Fabijanic, Z. Li, H. Chen, M. T. Mark, H. Molina, A. B. Martin, L. Bojmar, J. Fang, S. Rampersaud, A. Hoshino, I. Matei, C. M. Kenific, M. Nakajima, A. P. Mutvei, P. Sansone, W. Buehring, H. Wang, J. P. Jimenez, L. Cohen-Gould, N. Paknejad, M. Brendel, K. Manova-Todorova, A. Magalhães, J. A. Ferreira, H. Osório, A. M. Silva, A. Massey, J. R. Cubillos-Ruiz, G. Galletti, P. Giannakakou, A. M. Cuervo, J. Blenis, R. Schwartz, M. S. Brady, H. Peinado, J. Bromberg, H. Matsui, C. A. Reis, and D. Lyden, *Nat. Cell Biol.* **20**, 332 (2018).
- [71] J. Sloniec, M. Schnurr, C. Witte, U. Resch-Genger, L. Schröder, and A. Hennig, *Chem. - A Eur. J.* **19**, 3110 (2013).

- [72] M. Freemantle, *An Introduction to Ionic Liquids* (Royal Society of Chemistry, 2010).
- [73] B. N. Gantner, H. Singh, and R. D. Rogers, *Nat.* 2007 4477147 **447**, 917 (2007).
- [74] B. S. Phillips and J. S. Zabinski, *Tribol. Lett.* 2004 173 **17**, 533 (2004).
- [75] R. P. Swatloski, J. D. Holbrey, and R. D. Rogers, *Green Chem.* **5**, 361 (2003).
- [76] F. U. Shah, S. Glavatskih, P. M. Dean, D. R. MacFarlane, M. Forsyth, and O. N. Antzutkin, *J. Mater. Chem.* **22**, 6928 (2012).
- [77] F. U. Shah, S. Glavatskih, D. R. MacFarlane, A. Somers, M. Forsyth, and O. N. Antzutkin, *Phys. Chem. Chem. Phys.* **13**, 12865 (2011).
- [78] K. Damodaran, *Annu. Reports NMR Spectrosc.* **88**, 215 (2016).
- [79] A. Filippov, F. U. Shah, M. Taher, S. Glavatskih, and O. N. Antzutkin, *Phys. Chem. Chem. Phys.* **15**, 9281 (2013).
- [80] M. A. Javed, S. Ahola, P. Håkansson, O. Mankinen, M. K. Aslam, A. Filippov, F. U. Shah, S. Glavatskih, O. N. Antzutkin, and V.-V. Telkki, *Chem. Commun.* **53**, 11056 (2017).
- [81] T. Endo, M. Imanari, H. Seki, and K. Nishikawa, *J. Phys. Chem. A* **115**, 2999 (2011).
- [82] M. Urbańczyk, D. Bernin, W. Koźmiński, and K. Kazimierczuk, *Anal. Chem.* **85**, 1828 (2013).
- [83] K. E. Washburn and P. T. Callaghan, *Phys. Rev. Lett.* **97**, 175502 (2006).
- [84] Y. Q. Song, L. Venkataramanan, and L. Burcaw, *J. Chem. Phys.* **122**, 104104 (2005).
- [85] S. Ahola and V.-V. Telkki, *ChemPhysChem* **15**, 1687 (2014).
- [86] S. Ahola, V. V. Zhivonitko, O. Mankinen, G. Zhang, A. M. Kantola, H.-Y. Chen, C. Hilty, I. V. Koptug, and V.-V. Telkki, *Nat. Commun.* **6**, 8363 (2015).
- [87] G. Zhang, S. Ahola, M. H. Lerche, V.-V. Telkki, and C. Hilty, *Anal. Chem.* **90**, 11131 (2018).
- [88] J. N. King, V. J. Lee, S. Ahola, V.-V. Telkki, and T. Meldrum, *Angew. Chemie Int. Ed.* **55**, 5040 (2016).
- [89] Y. Shrot and L. Frydman, *J. Magn. Reson.* **195**, 226 (2008).
- [90] A. Tal and L. Frydman, *Prog. Nucl. Magn. Reson. Spectrosc.* **57**, 241 (2010).
- [91] V. V. Zhivonitko, M. S. Ullah, and V.-V. Telkki, *J. Magn. Reson.* **307**, 106571 (2019).

- [92] J. N. King, A. Fallorina, J. Yu, G. Zhang, V.-V. Telkki, C. Hilty, and T. Meldrum, *Chem. Sci.* **9**, 6143 (2018).
- [93] O. Mankinen, V. V Zhivonitko, A. Selent, S. Mailhot, S. Komulainen, N. L. Prisle, S. Ahola, and V.-V. Telkki, *Nat. Commun.* **11**, 3251 (2020).
- [94] M. S. Ullah, O. Mankinen, V. V. Zhivonitko, and V.-V. Telkki, *Phys. Chem. Chem. Phys.* **24**, 22109 (2022).

Original papers

1. Reproduced with permission from The Royal Society of Chemistry.
M. S. Ullah, V. V. Zhivonitko, A. Samoylenko, A. Zhyvolozhnyi, S. Viitala, S. Kankaanpää, S. Komulainen, L. Schröder, S. J. Vainio, and V.-V. Telkki, 2021.
Identification of extracellular nanoparticle subsets by nuclear magnetic resonance. *Chemical Science*, 12(24), 8311-8319.
2. Reproduced with permission from The Royal Society of Chemistry.
M. S. Ullah, O. Mankinen, V. V. Zhivonitko and V.-V. Telkki, 2022.
Ultrafast transverse relaxation exchange NMR spectroscopy. *Physical Chemistry Chemical Physics*, 24(36), 22109-22114.
3. Reproduced with permission from The Elsevier
V. V. Zhivonitko, M. S. Ullah and V.-V. Telkki, 2019.
Nonlinear sampling in ultrafast Laplace NMR. *Journal of Magnetic Resonance*, 307, 106571.

The original publications are not included in the electronic version of the dissertation.